Math. Model. Nat. Phenom.
Vol. 9, No. 6, 2014, pp. 117–141
DOI: 10.1051/mmnp/20149609

Blood Flow Simulation Using Traceless Variant of Johnson-Segalman Viscoelastic Model

T. Bodnár[1], M. Pires[2,3], J. Janela[4] *

[1] Faculty of Mechanical Engineering, Czech Technical University in Prague
Karlovo Náměstí 13, 121 35 Prague 2, Czech Republic

[2] Department of Mathematics and CIMA-UE, Évora University
Rua Romão Ramalho, 7000-671, Évora, Portugal

[3] CEMAT, Instituto Superior Técnico, Universidade de Lisboa
Av. Rovisco Pais 1, 1049-001 Lisboa, Portugal

[4]Department of Mathematics and CEMAPRE, ISEG, Universidade de Lisboa
Rua do Quelhas 6, 1200-781 Lisbon, Portugal

Abstract. A traceless variant of the Johnson-Segalman viscoelastic model is presented and applied to blood flow simulations. The viscoelastic extra stress tensor is decomposed into its traceless (deviatoric) and spherical parts, leading to a reformulation of the classical Johnson-Segalman model. The equivalence of the two models is established comparing model predictions for simple test cases. The new model is validated using several 2D benchmark problems, designed to reproduce difficulties that arise in the simulation of blood flow in blood vessels or medical devices. The structure and behaviour of the new model are discussed and the future use of the new model in envisioned, both on the theoretical and numerical perspectives.

Keywords and phrases: blood, viscoelastic, Johnson-Segalman, Oldroyd, traceless tensor

Mathematics Subject Classification: 76A10, 76M10, 74A10

1. Motivation

The incompressible Navier-Stokes model has been long used to describe blood flow in the human circulatory system, mainly due to simplicity of the involved assumptions. It describes an incompressible viscous fluid with Newtonian rheology. In this framework the stress tensor is naturally split into its spherical part (represented by pressure) and deviatoric (i.e. traceless) viscous part. These two components have different physical roles and are treated in a different way from the numerical point of view. Also, experimentally, these two stress components are measured by different procedures.

When instead of the Newtonian model more complicated non-Newtonian rheological constitutive models are used, this natural spherical/deviatoric splitting of the stress tensor is lost. In these models the computed pressure does not represent the whole spherical part of stress tensor. This is the case of the com-

*Corresponding author. E-mail: Tomas.Bodnar@fs.cvut.cz

© EDP Sciences, 2014

Article published by EDP Sciences and available at http://www.mmnp-journal.org or http://dx.doi.org/10.1051/mmnp/20149609
https://doi.org/10.1051/mmnp/20149609 Published online by Cambridge University Press

monly used class of differential viscoelastic models, such as the upper-convected Maxwell or Oldroyd-B models, both of them being special cases of the Johnson-Segalman model.

The aim of this paper is to reformulate the Johnson-Segalman model in order to recover the spherical/deviatoric stress tensor splitting into this class of differential viscoelastic models. This reformulation of the Johnson-Segalman model is referred to as the traceless formulation. This model was chosen because it contains the commonly used Maxwell and Oldroyd models as special cases. These viscoelastic models are often generalized (using variable viscosity or relaxation time) to describe the flow of blood and thus the methodology developed here for the Johnson-Segalman model is applicable to a much wider class of models being used for blood flow simulations.

Scope of the paper This paper is aimed at developing and validating a traceless variant of the Johnson-Segalman viscoelastic model. Being the first work dedicated to this topic, some numerical simulations are chosen to demonstrate the equivalence of the classical and traceless variants of the model in terms of results, also at the numerical level. This paper should be considered as an introductory study of the model. Issues related to practical applicability, computational efficiency and other possible properties of the newly developed variant of the model are beyond the scope of this initial part of our work.

Structure of the paper The work is organized into four sections. The introductory section contains a short overview of relevant blood rheology, mentioning models where this traceless decomposition can be applied. The second section, most important section is devoted to the description of the classical Johnson-Segalman model, the development of traceless variant of this model and its analytical solution in simple geometries and flow conditions. The next section contains numerical experiments validating the newly developed traceless model, by comparison with the classical version. The final section concludes the work by summarizing the numerical experiments and giving some outlook for future work on this subject.

2. Introduction

The simulation of flow of blood is one of the most challenging problems in contemporary Computational Fluid Dynamics (CFD). It is a complex flow problem, featuring many specific characteristics that have to be properly modelled and included in simulations. These characteristics include a complex rheological behaviour, flow pulsatility, complicated shape of flow domains, important fluid-structure interactions, influence of blood microstructure, changes in the blood behaviour on various space and time scales, significant patient-specific variations in blood properties and vessel geometry.

As a result, there is a wide range of models used to describe the behaviour of blood. None of them is generally accepted as a universal model capturing all the above mentioned phenomena. The model presented below focuses on non-Newtonian rheology of blood, emphasising the viscoelasticity of blood, as well as a possible extension to capture shear-thinning behaviour.

Non-Newtonian behaviour of blood Although in many studies blood is considered to be a Newtonian fluid, several important non-Newtonian characteristics can be observed in blood flow in certain circumstances. Among the most frequently considered non-Newtonian properties of blood we highlight the *shear-thinning viscosity*, *viscoelasticity* and *thixotropy*.

Among these three non-Newtonian features, the shear-thinning viscosity, i.e., the shear-rate dependent variation of apparent viscosity, is probably the most often discussed and taken into account. A very comprehensive overview of blood viscosity behaviour can be found e.g. in [12]. It is evident that the apparent viscosity of blood reduces with increasing shear rate. There are several factors contributing to this behaviour, mainly due to the formation and break-up of rouleaux (i.e., aggregation and disaggregation of red blood cells), and to the orientation and deformation of non-spherical cells in blood. Some experimental and numerical evidence of these effects was presented e.g. in [38].

The existence of yield-stress in blood flows was documented e.g. in [30]. The yield stress in blood depends mainly on *hematocrit* (i.e., red blood cells concentration) and fibrin concentration. This property

https://doi.org/10.1051/mmnp/20149609 Published online by Cambridge University Press

has to be considered in low-shear regions with large residence times, where the RBC's have enough time to aggregate. The yield-stress can either be considered separately, in a generalised Newtonian model with an appropriate shear-dependent viscosity function (like in the Bingham), or together with viscoelastic and thixotropic models [36], [39]. This led to development of blood flow models emphasising the importance of *thixotropy*. One such model is developed and used e.g. in [27].

Due to the micro-structure of blood it seems natural to consider blood as a *viscoelastic* fluid. The models mentioned or introduced in this paper aim at modelling this particular behaviour of blood.

Viscoelasticity of blood The viscoelastic properties of blood were measured in several experimental studies. One of the earliest was presented in [34, 35], followed later by [37]. The viscoelasticity can be seen as a consequence of microstructure of blood in which red blood cells, being elastic containers filled with a viscous fluid, aggregate to form larger chains (rouleaux) introducing an elastic stress component into an otherwise only viscous fluid. This behaviour is well known from polymeric fluid dynamics in which a specific class of micellar fluids is often considered to exhibit this kind of properties. Although the viscoelasticity of blood is apparent in many specific blood flow situations, it is seldom considered in mathematical blood flow models and numerical simulations. In our view, this option is motivated by saving the extra computational time necessary to solve the more complex viscoelastic models and is rarely based on rigorous measurements actually showing that the viscoelastic effects are negligible.

Viscoelastic models There is a wide range of different viscoelastic models, used in various applications of fluid dynamics. This is also the case of blood flow modelling and simulation. These models can be divided in three major classes, depending on how the viscoelastic extra stress tensor is evaluated depending on macroscopic or microscopic flow parameters. As a consequence, a different type of governing equation is obtained for the components of the extra stress tensor[1].

- *Statistical models* – The macroscopic rheological parameters are in this case evaluated using statistical methods coming up from micro-structural models dealing with interactions of cells, molecules and chains in the fluid. Typical examples of this class are the dumbbell models, FENE model and its variants taking into account the elastic stretching of polymeric chains within the fluid. These models are described e.g. in [6] and applied to blood flow in [33].
- *Integral models* – The rheological law is described using time-integrals over the history of fluid (parcel or particle) deformation, possibly considering other relevant factors. The resulting governing equations for the extra stress tensor are integral, following the stress/strain history of individual fluid parcels over their specific history i.e. their trajectory. For examples of such models see e.g. [5], [16].
- *Differential models* – The spatio-temporal evolution of the viscoelastic extra stress tensor is described by a partial differential equation. This is a coupled set of transport equations (in the Eulerian flow description) for the components of the extra stress tensor. Although this model has some limitations concerning the infinitesimal deformations of fluid, it is widely used because it uses similar type of formalism as the flow equations (momentum balance laws) which makes it easier to implement and solve with existing CFD codes. These models are described in detail e.g. in [5]. Specific modification for blood flow have been developed e.g. in [1].

Numerical simulations of blood flow Numerical simulation is a key element for the better understanding and prediction of non-Newtonian phenomena. In the last two decades, with an exponential increase of computational power available to researchers and clinical experts, an enormous number of numerical studies of blood flows have been conducted. These studies generally treat a specific blood flow feature and, consequently, in order to get general overview of the state of the art in this area, it is necessary to go through a large amount of specialised literature. Therefore we do not aim at making a representative review of published work in this area but simply to mention some publications relevant to the problem under analysis in this paper.

[1]This second order stress tensor has to be symmetric, therefore $d(d+1)/2$ independent stress components must be computed, where d is the space dimension

https://doi.org/10.1051/mmnp/20149609 Published online by Cambridge University Press

A large amount of non-Newtonian models describing blood flow have been tested e.g. in [8],[9], [10], [19], [4], covering mainly the shear-thinning and thixotropic nature of blood and extensive comparisons with the classical Newtonian flows.

The advances in computation power, medical imaging techniques and image reconstruction, allowed blood flow simulation in patient-specific geometries. Many models have been tested in these complex patient-specific geometries. For fundamental initial works we refer to Perktold [28, 29] and references therein. More recently, some effort has been directed towards sensitivity analysis of these simulations with respect to blood flow model and geometry (see [17, 18] and references therein).

Oldroyd-type differential viscoelastic models have been used for blood flow simulations e.g. in [25], [1], [9], [7]. Also, some finite-element studies of generalised Oldroyd-B fluids flow in vessel-like curved domains were published e.g. in [2, 3] or [31].

There are some basic features common to the different numerical methods for viscoelastic flows. Discretisation in space is usually performed with Galerkin methods or by collocation, reducing the problem to a finite-dimensional one. This type of discretisation is present in finite element methods (conforming, non conforming, mixed, hybrid, discontinuous), in spectral methods (Legendre or Chebyshev expansion) or in different finite volume schemes. Discretisation in time is normally performed with finite difference or fractional-step schemes. These methods lead to the solution of typically very large algebraic systems, whose solution often requires preconditioning obtained through operator splitting, multigrid or domain decomposition methods.

Regarding the use of finite-element methods for simulation of viscoelastic flows, they have been long used e.g. in [25], [22]. Focus has been put on the use of discontinuous elements and on iterative linearization methods for the fully coupled problem.

The numerical simulation of these flows poses some specific challenges related to limitations in the range of feasible Weissenberg numbers (non-dimensional number related to viscoelasticity). Several strategies have been designed to mitigate these problem, for example operator splitting methods like the elastic viscous split stress (EVSS), stabilisation methods (e.g. SUPG), different combinations of low and high order methods or discontinuous stresses.

3. Mathematical Model

3.1. Classical Johnson-Segalman Model

The equations of motion can be derived from the conservation (balance) laws for mass and linear momentum, supplemented by rheological constitutive relations for the stress tensor. The conservation of mass, which is in this case equivalent to an incompressibility constraint, can be written in differential form as

$$\mathrm{div}\boldsymbol{u} = 0 \tag{3.1}$$

The conservation of linear momentum reads

$$\rho\frac{D\boldsymbol{u}}{Dt} = \mathrm{div}\mathbf{T} - \nabla p \tag{3.2}$$

Here $\boldsymbol{u}$ stands for the fluid velocity vector, ρ is the density, p is the pressure. The stress tensor is denoted by $\mathbf{T}$. It should be noted that the pressure p should be regarded as a Lagrange multiplier enforcing the incompressibility constraint rather than a thermodynamical quantity as we know it from compressible fluid dynamics. For Newtonian fluids the stress tensor can be defined explicitly as $\mathbf{T} = 2\mu\mathbf{D}$ with μ being the dynamical viscosity. In this case the total stress tensor is already split into its traceless[2] (deviatoric) part $\mathbf{T}$ and spherical part $-p\mathbf{I}$.

The rheological constitutive model for the problems discussed below is based on the *Johnson-Segalman* model. This model has been extensively studied and used in the past, see e.g. [32], [23], [14], [15]. The

[2]The incompressibility constraint $\mathrm{div}\boldsymbol{u} = 0$ can be alternatively and equivalently expressed as $\mathrm{Tr}\mathbf{D} = 0$.

https://doi.org/10.1051/mmnp/20149609 Published online by Cambridge University Press

well known upper–convected, lower–convected and co–rotational Maxwell models as well as the Oldroyd–A and Oldroyd–B models are special sub-cases of the Johnson–Segalman class of models. In this case the stress tensor $\mathbf{T}$ consists in the Newtonian (solvent) part $\mathbf{T}_s$ and the viscoelastic part $\mathbf{T}_e$.

$$\mathbf{T} = \mathbf{T}_s + \mathbf{T}_e \tag{3.3}$$

These two stress components $\mathbf{T}_s$ and $\mathbf{T}_e$ are defined as Newtonian, resp. Maxwell fluids.

$$\mathbf{T}_s = 2\mu_s \mathbf{D} \tag{3.4}$$

$$\mathbf{T}_e + \lambda \frac{\delta \mathbf{T}_e}{\delta t} = 2\mu_e \mathbf{D} \tag{3.5}$$

The symbol $\mathbf{D}$ denotes the symmetric part of the velocity gradient. The physical parameters in this model are the solvent and elastic viscosities μ_s, resp. μ_e and the relaxation time λ.

Convected derivative(s)

The *convected derivative* $\frac{\delta \mathbf{T}_e}{\delta t}$ in the equation (3.5) can be chosen from the one-parametric family of *Gordon-Schowalter* derivatives given by :

$$\left(\frac{\delta \mathbf{T}_e}{\delta t}\right)_a = \frac{D\mathbf{T}_e}{Dt} - \mathbf{W}\mathbf{T}_e + \mathbf{T}_e\mathbf{W} + a(\mathbf{D}\mathbf{T}_e + \mathbf{T}_e\mathbf{D}) \qquad a \in [-1;1] \tag{3.6}$$

When $a = -1$, this corresponds to an upper convected derivative, $a = 0$ yields a co-rotational (or Jaumann) derivative and for $a = 1$ we get the lower convected derivative. The most commonly used Oldroyd-B (upper convected Maxwell) model is obtained when $a = -1$. Expanding the material time derivative $\frac{D}{Dt} = \frac{\partial}{\partial t} + \boldsymbol{u} \cdot \boldsymbol{\nabla}$ it is possible to rewrite equation (3.5) for the elastic stress tensor $\mathbf{T}_e$.

$$\frac{\partial \mathbf{T}_e}{\partial t} + (\boldsymbol{u} \cdot \boldsymbol{\nabla})\, \mathbf{T}_e = \frac{2\mu_e}{\lambda}\mathbf{D} - \frac{1}{\lambda}\mathbf{T}_e + (\mathbf{W}\mathbf{T}_e - \mathbf{T}_e\mathbf{W}) - a(\mathbf{D}\mathbf{T}_e + \mathbf{T}_e\mathbf{D}) \qquad a \in \langle -1;1\rangle \tag{3.7}$$

Classical model summary

The full Johnson-Segalman model can be written as:

$$\operatorname{div} \boldsymbol{u} = 0 \tag{3.8}$$

$$\frac{\partial \boldsymbol{u}}{\partial t} + (\boldsymbol{u} \cdot \boldsymbol{\nabla})\, \boldsymbol{u} = \frac{1}{\rho}\big[\operatorname{div}(\mathbf{T}_s + \mathbf{T}_e) - \nabla p\big] \tag{3.9}$$

$$\mathbf{T}_s = 2\mu_s \mathbf{D} \tag{3.10}$$

$$\frac{\partial \mathbf{T}_e}{\partial t} + (\boldsymbol{u} \cdot \boldsymbol{\nabla})\, \mathbf{T}_e = \frac{1}{\lambda}\left[2\mu_e \mathbf{D} - \mathbf{T}_e\right] + (\mathbf{W}\mathbf{T}_e - \mathbf{T}_e\mathbf{W}) - a(\mathbf{D}\mathbf{T}_e + \mathbf{T}_e\mathbf{D}) \tag{3.11}$$

The convected derivative parameter is in the range $a \in \langle -1;1\rangle$. The Newtonian fluid model (i.e. the Navier-Stokes equations) can be obtained in the limit of $\lambda \longrightarrow 0$. The Oldroyd-B model is obtained when $a = -1$. For $\mu_s = 0$ the Maxwell model is recovered.

3.2. Traceless Johnson-Segalman Model

Derivation of the traceless model

The elastic stress tensor $\mathbf{T}_e$ is described by the following evolution equation:

$$\frac{\partial \mathbf{T}_e}{\partial t} + (\boldsymbol{u} \cdot \boldsymbol{\nabla})\, \mathbf{T}_e = \frac{1}{\lambda}\left[2\mu_e \mathbf{D} - \mathbf{T}_e\right] + \underbrace{(\mathbf{W}\mathbf{T}_e - \mathbf{T}_e\mathbf{W})}_{\mathrm{Tr}=0} - a\underbrace{(\mathbf{D}\mathbf{T}_e + \mathbf{T}_e\mathbf{D})}_{\mathrm{Tr}\neq 0} \qquad a \in \langle -1;1\rangle \tag{3.12}$$

https://doi.org/10.1051/mmnp/20149609 Published online by Cambridge University Press

If the $\mathbf{T}_e$ is initialised by the traceless tensor field (e.g., $\mathbf{T}_e = c\mathbf{D}$), then only the last term on the right hand side of (3.12) will contribute for the trace $\mathrm{Tr}(\mathbf{T}_e)$.

The elastic stress tensor $\mathbf{T}_e$ can be decomposed[3] into its traceless (deviatoric) part $\mathbf{T}_e^{\square}$ and diagonal (spherical) part $\mathbf{T}_e^{\blacksquare}$.

$$\mathbf{T}_e = \mathbf{T}_e^{\square} + \mathbf{T}_e^{\blacksquare} \qquad \text{where} \qquad \mathbf{T}_e^{\blacksquare} = \frac{1}{\mathrm{Tr}(\mathbf{I})}\mathrm{Tr}(\mathbf{T}_e)\mathbf{I} \tag{3.13}$$

This decomposition (3.13) is introduced in the constitutive relation (3.12). The tensor products on the right hand side are decomposed in a similar way. The traceless part of each tensor is denoted by the superscript $\square$, while $\blacksquare$ is used for the remaining diagonal part. The terms on the right hand side of (3.12) should be decomposed as follows:

$$(\mathbf{D}\mathbf{T}_e + \mathbf{T}_e\mathbf{D}) = \underbrace{(\mathbf{D}\mathbf{T}_e^{\square} + \mathbf{T}_e^{\square}\mathbf{D})}_{\mathrm{Tr}\neq 0} + \underbrace{(\mathbf{D}\mathbf{T}_e^{\blacksquare} + \mathbf{T}_e^{\blacksquare}\mathbf{D})}_{=2\mathbf{T}_e^{\blacksquare}\mathbf{D};\ \mathrm{Tr}=0} \tag{3.14}$$

The term $(\mathbf{D}\mathbf{T}_e^{\square} + \mathbf{T}_e^{\square}\mathbf{D})$ is not traceless and thus it should be further decomposed:

$$(\mathbf{D}\mathbf{T}_e^{\square} + \mathbf{T}_e^{\square}\mathbf{D}) = (\mathbf{D}\mathbf{T}_e^{\square} + \mathbf{T}_e^{\square}\mathbf{D})^{\square} + \underbrace{(\mathbf{D}\mathbf{T}_e^{\square} + \mathbf{T}_e^{\square}\mathbf{D})^{\blacksquare}}_{=2(\mathbf{T}_e^{\square}\mathbf{D})^{\blacksquare}} \tag{3.15}$$

In a similar way (for $\mathbf{W}$ being skew-symmetric and $\mathbf{T}_e^{\blacksquare}$ symmetric) the expression $(\mathbf{W}\mathbf{T}_e - \mathbf{T}_e\mathbf{W})$ can further be simplified:

$$(\mathbf{W}\mathbf{T}_e - \mathbf{T}_e\mathbf{W}) = (\mathbf{W}\mathbf{T}_e^{\square} - \mathbf{T}_e^{\square}\mathbf{W}) + \underbrace{(\mathbf{W}\mathbf{T}_e^{\blacksquare} - \mathbf{T}_e^{\blacksquare}\mathbf{W})}_{0} = (\mathbf{W}\mathbf{T}_e - \mathbf{T}_e\mathbf{W})^{\square} \tag{3.16}$$

The evolution of the traceless part $\mathbf{T}_e^{\square}$ is then governed by:

$$\frac{\partial \mathbf{T}_e^{\square}}{\partial t} + (\boldsymbol{u}\cdot\boldsymbol{\nabla})\,\mathbf{T}_e^{\square} = \frac{1}{\lambda}\left[2\mu_e\mathbf{D} - \mathbf{T}_e^{\square}\right] + (\mathbf{W}\mathbf{T}_e - \mathbf{T}_e\mathbf{W})^{\square} - a(\mathbf{D}\mathbf{T}_e + \mathbf{T}_e\mathbf{D})^{\square} \tag{3.17}$$

Using relations (3.14), (3.16) and (3.15), the equation (3.17) can be rewritten into its (almost) final form:

$$\frac{\partial \mathbf{T}_e^{\square}}{\partial t} + (\boldsymbol{u}\cdot\boldsymbol{\nabla})\,\mathbf{T}_e^{\square} = \frac{1}{\lambda}\left[2\mu_e\mathbf{D} - \mathbf{T}_e^{\square}\right] + (\mathbf{W}\mathbf{T}_e^{\square} - \mathbf{T}_e^{\square}\mathbf{W}) - a\underbrace{(\mathbf{D}\mathbf{T}_e^{\square} + \mathbf{T}_e^{\square}\mathbf{D})^{\square}}_{=0\ in\ 2D} - 2a\mathbf{T}_e^{\blacksquare}\mathbf{D} \tag{3.18}$$

It can be easily seen that one of the terms on the right hand side vanishes in purely two-dimensional flows.

The equation for the diagonal part $\mathbf{T}_e^{\blacksquare}$ is simpler, because $(\mathbf{W}\mathbf{T}_e - \mathbf{T}_e\mathbf{W})^{\blacksquare} = \mathbf{0}$.

$$\frac{\partial \mathbf{T}_e^{\blacksquare}}{\partial t} + (\boldsymbol{u}\cdot\boldsymbol{\nabla})\,\mathbf{T}_e^{\blacksquare} = -\frac{1}{\lambda}\mathbf{T}_e^{\blacksquare} - a\underbrace{(\mathbf{D}\mathbf{T}_e^{\square} + \mathbf{T}_e^{\square}\mathbf{D})^{\blacksquare}}_{=2(\mathbf{T}_e^{\square}\mathbf{D})^{\blacksquare}} \tag{3.19}$$

The decomposed system of tensor equations for the elastic stress can be written as:

$$\frac{\partial \mathbf{T}_e^{\square}}{\partial t} + (\boldsymbol{u}\cdot\boldsymbol{\nabla})\,\mathbf{T}_e^{\square} = \frac{1}{\lambda}\left[2\mu_e\mathbf{D} - \mathbf{T}_e^{\square}\right] + (\mathbf{W}\mathbf{T}_e^{\square} - \mathbf{T}_e^{\square}\mathbf{W}) - a(\mathbf{D}\mathbf{T}_e^{\square} + \mathbf{T}_e^{\square}\mathbf{D})^{\square} - 2a\mathbf{T}_e^{\blacksquare}\mathbf{D} \tag{3.20}$$

$$\frac{\partial \mathbf{T}_e^{\blacksquare}}{\partial t} + (\boldsymbol{u}\cdot\boldsymbol{\nabla})\,\mathbf{T}_e^{\blacksquare} = -\frac{1}{\lambda}\mathbf{T}_e^{\blacksquare} - 2a(\mathbf{T}_e^{\square}\mathbf{D})^{\blacksquare} \tag{3.21}$$

In this system of equations the stress components $\mathbf{T}_e^{\square}$ and $\mathbf{T}_e^{\blacksquare}$ only appear separately. The separate systems governing their evolution are linked to each other (also to momentum equations) via the last term on the right hand side. It seems that we have now twice the number of original tensor equations, but:

[3] In fact any tensor can be decomposed in such a way.

https://doi.org/10.1051/mmnp/20149609 Published online by Cambridge University Press

– From the system (3.20) only *5 components* (in 3D) need to be computed, while the last (diagonal) component can be obtained by applying the definition $\mathrm{Tr}(\mathbf{T}_e^{\square}) = 0$.
– The equation (3.21) is in fact only a scalar evolution equation for the trace of $\mathbf{T}_e$. This is due to specific structure of $\mathbf{T}_e^{\blacksquare}$ given by the definition $\mathbf{T}_e^{\blacksquare} = \frac{1}{\mathrm{Tr}(\mathbf{I})}\mathrm{Tr}(\mathbf{T}_e)\mathbf{I}$.

The $\mathrm{Tr}(\mathbf{T}_e)$ plays a role similar to pressure. Based on this observation a new *elastic pressure* variable p_e can be defined as:

$$\mathbf{T}_e^{\blacksquare} = -p_e\mathbf{I} \qquad \Longrightarrow \qquad p_e = -\frac{1}{\mathrm{Tr}(\mathbf{I})}\mathrm{Tr}(\mathbf{T}_e) = -\frac{1}{\mathrm{Tr}(\mathbf{I})}\mathrm{Tr}(\mathbf{T}_e^{\blacksquare}) \tag{3.22}$$

From (3.21) follows the evolution equation for elastic pressure:

$$\frac{\partial p_e}{\partial t} + (\boldsymbol{u}\cdot\boldsymbol{\nabla})\, p_e = -\frac{1}{\lambda}p_e + \frac{2a}{\mathrm{Tr}(\mathbf{I})}\mathrm{Tr}(\mathbf{T}_e^{\square}\mathbf{D}) \tag{3.23}$$

Finally instead of the original governing system in 3D case for (6 components of) $\mathbf{T}_e$, we end up with a system of equations for (5 components of) $\mathbf{T}_e^{\square}$ and (1 scalar) equation for elastic pressure p_e.

The elastic pressure equation (3.23) deserves some attention. The first (sink) term on the right hand side is responsible for an exponential decay in time of the (magnitude of) the elastic pressure. The rate of decay is determined by the relaxation time λ. The second (source) term contains the expression $\mathrm{Tr}(\mathbf{T}_e^{\square}\mathbf{D}) = \mathbf{T}_e^{\square} : \mathbf{D}$ which is part of the quantity usually called *stress power* and is related to the energy stored in fluid (material) due to stress. In the case of an undeformed velocity field in which $\mathbf{D} = \mathbf{0}$, the equation reduces to a simple transport equation $\frac{Dp_e}{Dt} = -\frac{1}{\lambda}p_e$ leading to exponential decay of p_e along a streamline. The equation also shows (together with equation (3.20)) that the elastic pressure p_e cannot be shifted by a constant as its incompressible counterpart p.

Traceless model summary

The full new traceless model can be written as

$$\mathrm{div}\,\boldsymbol{u} = 0 \tag{3.24}$$

$$\frac{\partial \boldsymbol{u}}{\partial t} + (\boldsymbol{u}\cdot\boldsymbol{\nabla})\,\boldsymbol{u} = \frac{1}{\rho}\big[\mathrm{div}(\mathbf{T}_s + \mathbf{T}_e^{\square}) - \nabla(p + p_e)\big] \tag{3.25}$$

$$\mathbf{T}_s = 2\mu_s\mathbf{D} \tag{3.26}$$

$$\frac{\partial \mathbf{T}_e^{\square}}{\partial t} + (\boldsymbol{u}\cdot\boldsymbol{\nabla})\mathbf{T}_e^{\square} = \frac{1}{\lambda}\left[2\mu_e\mathbf{D} - \mathbf{T}_e^{\square}\right] + (\mathbf{W}\mathbf{T}_e^{\square} - \mathbf{T}_e^{\square}\mathbf{W}) - a(\mathbf{D}\mathbf{T}_e^{\square} + \mathbf{T}_e^{\square}\mathbf{D})^{\square} + 2ap_e\mathbf{D} \tag{3.27}$$

$$\frac{\partial p_e}{\partial t} + (\boldsymbol{u}\cdot\boldsymbol{\nabla})\, p_e = -\frac{1}{\lambda}p_e + \frac{2a}{\mathrm{Tr}(\mathbf{I})}\mathrm{Tr}(\mathbf{T}_e^{\square}\mathbf{D}) \tag{3.28}$$

By comparison with the original version of the model we conclude that the new traceless model is slightly simpler when it comes to the evaluation of the right hand sides of equations. The reduction of the number of terms to be computed is even more apparent in 2D case when (as noted earlier) some more terms will vanish from the equation for $\mathbf{T}_e^{\square}$.

3.3. Analytical solution for Poiseuille flow

In the case of Poiseuille flow, i.e., fully developed flow in a straight channel (pipe), an analytical solution can be obtained. Such solutions for Johnson-Segalman model can be found e.g. in [5]. Here we will only focus on the solution of the traceless variant of the model.

The traceless elastic stress tensor components of $\mathbf{T}_e^{\square}$ are denoted[4] according to the following scheme:

$$\mathbf{T}_e^{\square} = \begin{pmatrix} \hat{t}_1 & \hat{t}_2 & \hat{t}_3 \\ \hat{t}_2 & \hat{t}_4 & \hat{t}_5 \\ \hat{t}_3 & \hat{t}_5 & \hat{t}_6 \end{pmatrix} \qquad \text{in 3D, resp.} \qquad \mathbf{T}_e^{\square} = \begin{pmatrix} \hat{t}_1 & \hat{t}_2 \\ \hat{t}_2 & \hat{t}_4 \end{pmatrix} \qquad \text{in 2D}$$

[4]The hat symbol $\hat{}$ is used to distinguish the new, traceless tensor components from the original tensor $\mathbf{T}_e$.

https://doi.org/10.1051/mmnp/20149609 Published online by Cambridge University Press

Traceless model in 2D

The governing equation for the elastic extra stress in 2D can be written in the following form:

$$\frac{\partial \mathbf{T}_e^{\square}}{\partial t} + (\boldsymbol{u}\cdot\boldsymbol{\nabla})\,\mathbf{T}_e^{\square} = \frac{1}{\lambda}\left[2\mu_e\mathbf{D} - \mathbf{T}_e^{\square}\right] + (\mathbf{W}\mathbf{T}_e^{\square} - \mathbf{T}_e^{\square}\mathbf{W}) + 2a(p_e\mathbf{D}) \tag{3.29}$$

$$\frac{\partial p_e}{\partial t} + (\boldsymbol{u}\cdot\boldsymbol{\nabla})\,p_e = -\frac{1}{\lambda}p_e + a\mathrm{Tr}(\mathbf{T}_e^{\square}\mathbf{D}) \tag{3.30}$$

The velocity vector only has an axial component and it is assumed to depend just on the y coordinate, i.e. $\boldsymbol{u} = (u(y), 0)$. The velocity gradient $\mathbf{L}$, and its symmetric resp. skew-symmetric components $\mathbf{D}$ resp. $\mathbf{W}$ will take the following specific form:

$$\mathbf{L} = \boldsymbol{\nabla}\boldsymbol{u} = \begin{pmatrix} 0 & u_y \\ 0 & 0 \end{pmatrix} \qquad \mathbf{D} = \frac{1}{2}\begin{pmatrix} 0 & u_y \\ u_y & 0 \end{pmatrix} \qquad \mathbf{W} = \frac{1}{2}\begin{pmatrix} 0 & u_y \\ -u_y & 0 \end{pmatrix}$$

Taking into account that the material time-derivatives on the left-hand side will vanish in Poiseuille type flow, the governing equations (3.31)-(3.32) can be reduced to:

$$\mathbf{T}_e^{\square} = 2\mu_e\mathbf{D} + \lambda\left[\mathbf{W}\mathbf{T}_e^{\square} + (\mathbf{W}\mathbf{T}_e^{\square})^T\right] + 2\lambda a(p_e\mathbf{D}) \tag{3.31}$$

$$p_e = \lambda a(\mathbf{T}_e^{\square} : \mathbf{D}) \tag{3.32}$$

Writing these equations component-wise they take the form:

$$\begin{pmatrix} \hat{t}_1 & \hat{t}_2 \\ \hat{t}_2 & \hat{t}_4 \end{pmatrix} = \mu_e\begin{pmatrix} 0 & u_y \\ u_y & 0 \end{pmatrix} + \frac{\lambda}{2}\begin{pmatrix} 2\hat{t}_2u_y & (\hat{t}_4-\hat{t}_1)u_y \\ (\hat{t}_4-\hat{t}_1)u_y & -2\hat{t}_2u_y \end{pmatrix} + \underbrace{\lambda^2a^2\hat{t}_2\begin{pmatrix} 0 & u_y^2 \\ u_y^2 & 0 \end{pmatrix}}_{2\lambda a p_e\mathbf{D}} \tag{3.33}$$

$$p_e = \lambda a\hat{t}_2u_y \tag{3.34}$$

After some calculations it is possible to obtain expressions for elastic stress tensor components $\hat{t}_1$, $\hat{t}_2$, $\hat{t}_4$ and elastic pressure p_e as functions of u_y.

$$\hat{t}_1 = \frac{\lambda\mu_e u_y^2}{1+(1-a^2)\lambda^2u_y^2} = -\hat{t}_4 \tag{3.35}$$

$$\hat{t}_4 = -\frac{\lambda\mu_e u_y^2}{1+(1-a^2)\lambda^2u_y^2} = -\hat{t}_1 \tag{3.36}$$

$$\hat{t}_2 = \frac{\mu_e u_y}{1+(1-a^2)\lambda^2u_y^2} \tag{3.37}$$

$$p_e = \frac{\lambda a\mu_e u_y^2}{1+(1-a^2)\lambda^2u_y^2} \tag{3.38}$$

The solution confirms that $\hat{t}_1 = -\hat{t}_4$. It also corresponds (after transformation) to the solution of the original model. Further observation reveals that the simple shear viscosity defined as

$$\widetilde{\mu_e}(u_y) = \frac{\hat{t}_2}{u_y} = \frac{\mu_e}{1+(1-a^2)\lambda^2u_y^2}, \tag{3.39}$$

i.e.,depends on the velocity gradient (i.e., shear rate). Only for $a = \pm 1$ it is constant, being equal to μ_e. For all the other intermediate values of the parameter $a \in (-1;1)$ the model predicts shear-thinning viscosity. This is a well known property of Johnson-Segalman model. For Oldroyd A and B models it plays no role, because these are obtained for $a = 1$, resp. $a = -1$.

The elastic pressure in this case has always the sign of the parameter a and vanishes on the axis of the vessel (pipe or channel). It can be explicitly computed if tensors $\mathbf{T}_e^{\square}$ and $\mathbf{D}$ are known.

https://doi.org/10.1051/mmnp/20149609 Published online by Cambridge University Press

It is also good to note that in the case $a = \pm 1$ the velocity field is the same as for the Newtonian case with viscosity $(\mu_s + \mu_e)$, i.e. the velocity has the classical parabolic profile. For all the other values of $a \in (-1; 1)$ the velocity profile is not known explicitly, but still the stress components can be computed from velocity gradient u_y for any given velocity profile.

3.4. Generalization to Shear-thinning viscosity

As it was already mentioned in section 2, in most flow regimes blood exhibits a shear-thinning behaviour. This property is well represented in the Johnson-Segalman model for parameter a in the range $a \in (-1, 1)$. This was demonstrated in the previous paragraphs leading to the shear dependent viscosity of the form shown in the equation (3.39). Although it is possible to use the Johnson-Segalman model in its shear-thinning regime (i.e. with parameter $a \neq \pm 1$), the more common approach is to use the (constant viscosity) Oldroyd-B model (i.e. to set $a = -1$) and generalize it by introducing an explicit formula for shear-thinning apparent viscosity, normally obtained by fitting experimental viscosity data. This approach was used e.g. in [7–9] or [25].

In order to account for the shear-thinning behavior of blood, the constant viscosity coefficient μ_s in (3.10) or (3.26) is replaced by a shear rate dependent viscosity function $\mu_s(\dot{\gamma})$

$$\mathbf{T}_s = 2\mu_s(\dot{\gamma})\mathbf{D} \quad . \tag{3.40}$$

One of the most frequently used shear-thinning models for blood is the generalized *Cross* model given by

$$\mu_s(\dot{\gamma}) = \mu_\infty + \frac{\mu_0 - \mu_\infty}{(1 + (\Lambda\dot{\gamma})^\beta)^\alpha}. \tag{3.41}$$

where *shear rate* is defined by $\dot{\gamma} = 2\sqrt{\mathbf{D} : \mathbf{D}}$. Here μ_0 and μ_∞ are the asymptotic viscosity values at zero and infinite shear rates. The following parameters found in [25] have been used for the blood flow simulations presented in this paper:

$$\begin{array}{cc} \mu_0 = 1.6 \cdot 10^{-1} Pa \cdot s & \mu_\infty = 3.6 \cdot 10^{-3} Pa \cdot s \\ \alpha = 1.23,\ \beta = 0.64 & \Lambda = 8.2 s \end{array}$$

It is evident, that this modification (generalization) of the model does not have any impact on the traceless splitting and can therefore be used with the original as well as with the traceless variants of Johnson-Segalman (resp. Oldroyd-B or Maxwell) model.

4. Numerical Experiments

The numerical experiments presented within this section are designed to illustrate, also at the numerical level, the equivalence of the classical and traceless variants of Johnson-Segalman model. Among the infinitely many possible parameter set-ups, the Oldroyd-B model (i.e. the case with $a = -1$) was chosen for simulations as it is the most commonly used model among the class of Johnson-Segalman models. In order to make use of the available analytical solution, some tests were performed without the (straightforward) shear-thinning generalization of the model. The shear-thinning Oldroyd-B model, applicable directly to blood flow, is used in the last computational case with a simple stenosed vessel. It should be noted that the numerical tests presented in this paper were performed to validate the newly developed model and thus no detailed studies of computational efficiency or stability with respect to Weissenberg number were performed. Any such study will require a model specific adjustments of numerical solver which is beyond the scope of this paper.

4.1. Numerical Method

Only a short description of the numerical algorithms used to obtain the presented results is given here. A decoupled scheme is used to solve the mixed elliptic-hyperbolic problem. The extra-stress tensor is computed separately from the kinematic equations. The solution of a Stokes problem provides the

https://doi.org/10.1051/mmnp/20149609 Published online by Cambridge University Press

initial kinematics and from this solution the viscoelastic extra-stress is computed. Next, the kinematics is updated with the current extra-stress, whose components are treated as known body-forces. This iterative process is a Picard's iterative scheme. The material derivative $\frac{D}{Dt} = \frac{\partial}{\partial t} + \boldsymbol{u} \cdot \boldsymbol{\nabla}$ is discretised by a weak form of the method of characteristics. Each time step corresponds to an iteration of the decoupled method.

4.2. Finite element Method

Let Ω be a bounded, open and connected Lipschitz domain in $\mathbb{R}^2$. We denote by $\mathcal{T}_h$ a non-degenerated triangulation of Ω. For each triangle $K \in \mathcal{T}_h$, we take its diameter h_K and define the diameter of the mesh, $h = \max_{K \in \mathcal{T}_h} h_K$. We define $\overline{\Omega} = \bigcup_{K \in \mathcal{T}_h} K$. Assuming that the triangles have approximately the same size, i.e., there exist positive constants C_1 and C_2 , independent of h, such that $C_1 h \leq h_K \leq C_2 \rho_K, \quad \forall K \in \mathcal{T}_h$ where ρ_K is the diameter of the greatest ball inscribed circle into K. Let $\mathbb{P}_k$ be the polynomial space from $\mathbb{R}^2$ into $\mathbb{R}$ of degree less than or equal to k and $\mathbb{P}_k(K)$ the restriction to $K \in \mathcal{T}_h$ of $\mathbb{P}_k$. To satisfy the LBB condition [20], we define the Hood-Taylor finite element space for $\boldsymbol{u}$ and p, respectively

$$\boldsymbol{V}_h = \left\{ v_h \in C\left(\overline{\Omega}\right) \cap \boldsymbol{H}_0^1\left(\Omega\right) : v_{h|K} \in \mathbb{P}_2\left(K\right), \ \forall K \in \mathcal{T}_h \right\}$$

$$M_h = \left\{ q_h \in C\left(\overline{\Omega}\right) \cap L_0^2\left(\Omega\right) : q_{h|K} \in \mathbb{P}_1\left(K\right), \ \forall K \in \mathcal{T}_h \right\}$$

For the discretisation of extra-stress tensor, we consider the discontinuous Galerkin method. The first discontinuous Galerkin method for hyperbolic partial differential equations was introduced in 1973 by Reed and Hill, to simulate neutron transport problem. The analysis of the abstract form for this discrete problem was done one year later by Lesaint and Raviart [24]. More recently, the discontinuous Galerkin method for hyperbolic equations had a significant development based on numerical fluxes [11]. The discontinuous Galerkin method can be viewed as a finite element method, but with relaxed continuity at inter-element boundaries. The key idea of the method is that the shape functions can be chosen so that the field variable and/or its derivatives are discontinuous across the element boundaries. The effects of the boundary conditions are gradually propagated through element-by-element connection. The details of this method can be found in [13, 24, 26].

To use this method in our formulation we introduce the discontinuous finite element space of piecewise quadratic functions

$$\boldsymbol{X}_h = \left\{ \tau_h \in L_2\left(\Omega\right) : \tau_{h|K} \in \mathbb{P}_2\left(K\right), \ \ \forall K \in \boldsymbol{T}_h \right\}$$

Following Ern and Guermond [13], we introduce the operator defined in $\boldsymbol{V}_h \times X_h \times X_h$

$$\mathcal{B}_h(\boldsymbol{u}_h, v_h, w_h) = \int_{\boldsymbol{T}_h} \left(\frac{1}{\lambda} v_h + \boldsymbol{u}_h \cdot \nabla v_h \right) \cdot w_h + \sum_{K \in \mathcal{F}_h^i} \int_{\partial K} \frac{1}{2} \left(|\boldsymbol{n} \cdot \boldsymbol{u}_h| - \boldsymbol{n} \cdot \boldsymbol{u}_h \right) [v_h] \, w_h - \int_{\boldsymbol{\Gamma}_h^{in}} |\boldsymbol{n} \cdot \boldsymbol{u}_h| v_h \cdot w_h$$

and for all symmetric tensors whose components belong X_h, we have an analogous operator defined in $\boldsymbol{V}_h \times X_h^{2\times 2} \times X_h^{2\times 2}$ by

$$\widetilde{\boldsymbol{\mathcal{B}}_h}(\boldsymbol{u}_h, \boldsymbol{\sigma_h}, \boldsymbol{\tau}_h) = \int_{\boldsymbol{T}_h} \left(\frac{1}{\lambda} \boldsymbol{\sigma_h} + \boldsymbol{u}_h : \nabla \sigma_h \right) : \boldsymbol{\tau}_h + \sum_{K \in \mathcal{F}_h^i} \int_{\partial K} \frac{1}{2} \left(|\boldsymbol{n} \cdot \boldsymbol{u}_h| - \boldsymbol{n} \cdot \boldsymbol{u}_h \right) [\sigma_h] : \boldsymbol{\tau}_h - \int_{\boldsymbol{\Gamma}_h^{in}} |\boldsymbol{n} \cdot \boldsymbol{u}_h| \boldsymbol{\sigma}_h : \boldsymbol{\tau}_h$$

https://doi.org/10.1051/mmnp/20149609 Published online by Cambridge University Press

where $[\boldsymbol{w}] = \boldsymbol{w}_{|K_1}\boldsymbol{n}_{K_1} + \boldsymbol{w}_{|K_2}\boldsymbol{n}_{K_2}$ denotes the jump of $\boldsymbol{w}$ across the edges of an element over which it is evaluated with $\boldsymbol{n}_{K_i}$ is the unit normal vector on the interface $\mathcal{F} = \partial K_1 \cap \partial K_2$ pointing exterior to K_i, $(i = 1, 2)$ and $\mathcal{F}_h^i$ is the set of interfaces. Observe that, for all γ admissible, the interface flux $\frac{1}{2}\left(|\boldsymbol{n}\cdot\boldsymbol{u}_h| - \boldsymbol{n}\cdot\boldsymbol{u}_h\right)[\gamma]$ is nonzero only on inflow boundary of K, i.e., $\partial K^-(\boldsymbol{u}_h)=\{\boldsymbol{x}\in\partial K : u_h(x)\cdot\boldsymbol{n}(x) < 0\}$.
We define the bilinear form in $\boldsymbol{V}_h \times \boldsymbol{V}_h$ and linear form in $M_h \times \boldsymbol{V}_h$, respectively by

$$a_h\left(\boldsymbol{u}_h, \boldsymbol{v}_h\right) = \frac{1}{\rho}\int_{\boldsymbol{T}_h} 2\mu_e \mathbf{D}\left(\boldsymbol{u}_h\right) : \mathbf{D}\left(\boldsymbol{v}_h\right) \qquad \text{and} \qquad b_h\left(p_h, \boldsymbol{v_h}\right) = \int_{\boldsymbol{T}_h} p_h \nabla\cdot\boldsymbol{v}_h.$$

The system (3.24)-(3.28) (2D) is approximated by the following problem:

Find $\left(\boldsymbol{u}_h, p_h, \mathbf{T}_{e\ h}^{\square}, p_{e,h}\right) = \left(\boldsymbol{u}, p, \mathbf{T}_e^{\square}, p_e\right) \in \boldsymbol{V}_h \times M_h \times \left[X_h\right]^{2\times 2} \times X_h$ solution of

$$\begin{cases} \int_{\boldsymbol{T}_h} \frac{D\boldsymbol{u}}{Dt} : \boldsymbol{v} + a_h\left(\boldsymbol{u}, \boldsymbol{v}\right) - b_h\left(p, \boldsymbol{v}\right) - b_h\left(q, \boldsymbol{u}\right) = \int_{\boldsymbol{T}_h} \nabla\cdot\mathbf{T}_e^{\square} : \boldsymbol{v} - \int_{\boldsymbol{T}_h} \nabla p_e \cdot \boldsymbol{v} \\ \int_{\boldsymbol{T}_h} \frac{\partial \mathbf{T}_e^{\square}}{\partial t} : \boldsymbol{\tau} + \widetilde{\mathcal{B}_h}\left(\boldsymbol{u}\mathbf{T}_e^{\square}, \boldsymbol{\tau}\right) = \int_{\boldsymbol{T}_h} \left[\frac{2\mu_e}{\lambda}\mathbf{D}\left(\boldsymbol{u}\right) + \left(\mathbf{W}\left(\boldsymbol{u}\right)\mathbf{T}_e^{\square} - \mathbf{T}_e^{\square}\mathbf{W}\left(\boldsymbol{u}\right)\right) + 2ap_e\mathbf{D}\left(\boldsymbol{u}\right)\right] : \boldsymbol{\tau} \\ \int_{\boldsymbol{T}_h} \frac{\partial p_e}{\partial t} q_e + \mathcal{B}_h\left(\boldsymbol{u}, p_e, q_e\right) = \int_{\boldsymbol{T}_h} Tr(\mathbf{T}_e^{\square}\mathbf{D}(\boldsymbol{u}))q_e \end{cases}$$

for all $(v, q, \boldsymbol{\tau}, q_e) \in \boldsymbol{V}_h \times M_h \times \left[X_h\right]^{2\times 2} \times X_h$

4.3. Computational Setup

To investigate the equivalence between the classical Johnson-Segalman model and the traceless model we developed a code in 2D using the finite element software package FreeFem++ [21]. The linear systems are solved using the Crout matrix decomposition for the kinematics and a GMRES solver to obtain the tensor and elastic pressure. As described in the previous section, continuous piecewise elements of order 2 are used for the velocity, continuous piecewise elements of order 1 are used for the pressure and discontinuous piecewise elements of order 2 are used for the tensor and elastic pressure.

4.3.1. Poiseuille flow

The straight pipe (vessel) was chosen to compare the numerical solution with the analytical one for all models. The point is to provide some basic validation of the models and the information about the structure of the resulting fields.

Case geometry The straight vessel of finite length is characterised by its cross-sectional dimension $D = 6.2mm$ and length $L = 20D$.

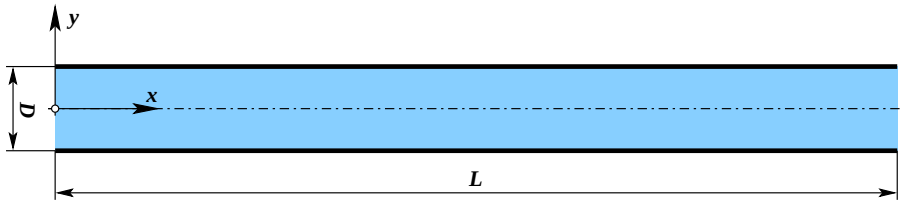


FIGURE 1. Geometry definition for the Poiseuille flow (straight vessel).

Computational grid The grid is unstructured with triangular elements. The final grid consists of approximately 9000 elements. This grid is adapted during the simulation to capture high gradients in the computational field.

https://doi.org/10.1051/mmnp/20149609 Published online by Cambridge University Press

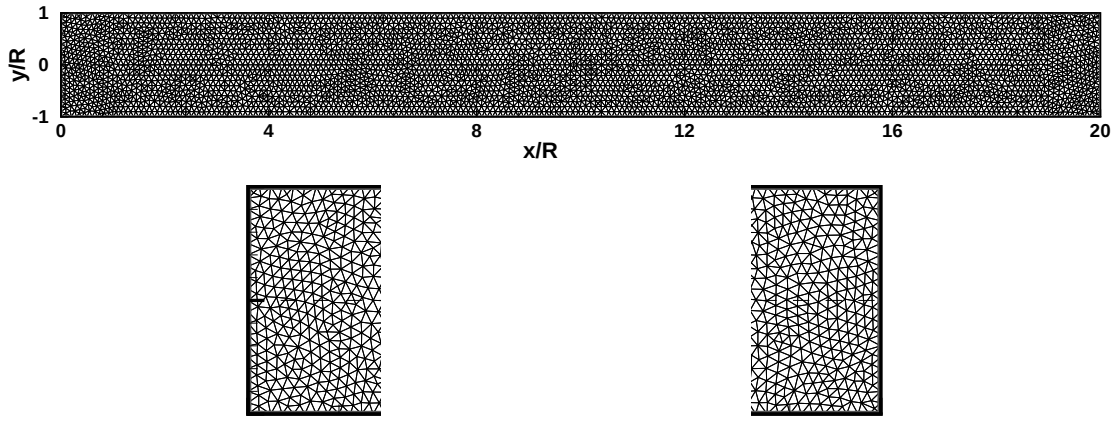


FIGURE 2. Grid for the Poiseuille flow (straight vessel).

Boundary conditions We prescribe boundary conditions on the solid wall and on the upstream region. On the solid wall no-slip conditions are imposed. On the upstream boundary $\partial\Omega^{-}(\boldsymbol{u}) = \{\mathbf{x} \in \partial\Omega : \boldsymbol{u}(\boldsymbol{x}) \cdot \boldsymbol{n}(\boldsymbol{x}) < 0\}$ we imposed the known analytical solution for the fully developed flow in a straight channel (pipe). The classical Johnson-Segalman model can be found e.g. in [5]. For the traceless model the solution is given by (3.35)–(3.38).

4.3.2. Flow in corrugated vessel

Case geometry The corrugated vessel is assumed to consist on straight inlet and outlet parts with dimension[5] of D. The attached contraction/expansion parts have length L_{con}, L_{exp}. Between these parts, several identical segments are inserted. These segments are characterised by its minimum and maximum diameters D_{min} resp. D_{max} and the length L_{seg}. All the curvilinear walls have *sinusoidal* shape. The configuration of such corrugated vessel is shown in the figure 3.

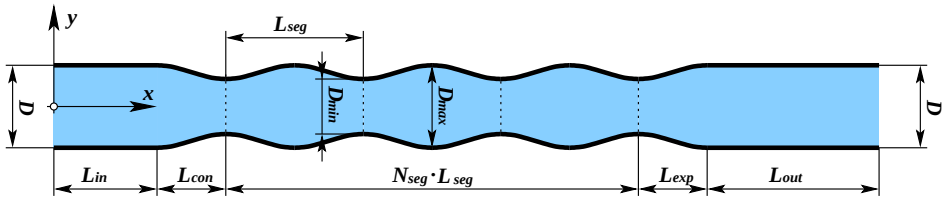


FIGURE 3. Geometry definition for the corrugated vessel case.

The dimensions used for this case closely follow the Poiseuille flow test case. The diameter (cross-section) size $D = 6.2mm$ is used to define other characteristic lengths.

$D_{max} = D$	$L_{con} = L_{seg}/2$	$L_{in} = 3D$	$N_{seg} = 3$
$D_{min} = D/\sqrt{2}$	$L_{exp} = L_{seg}/2$	$L_{out} = 5D$	$L_{seg} = 2D$

TABLE 1. Corrugated vessel dimensions.

[5]Diameter in 3D

https://doi.org/10.1051/mmnp/20149609 Published online by Cambridge University Press

Computational grid The grid has only about 3000 elements. No special treatment was used to symmetrize the grid with respect to x axis.

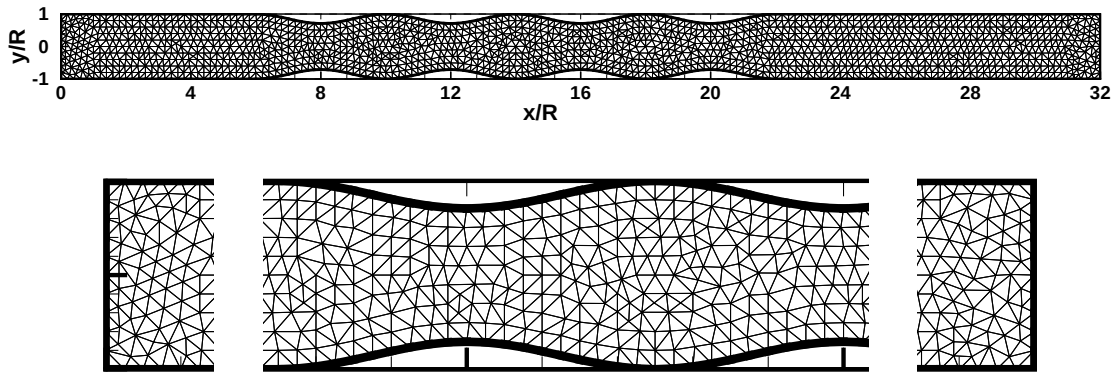


FIGURE 4. Grid for the corrugated vessel flow.

Boundary conditions The computational domain has a length of straight inlet and outlet pipe sufficiently long to obtain a fully developed Poiseuille flow upstream and downstream. On the upstream boundary the analytical solution for the fully developed flow in a straight pipe for the respective model are imposed. On the solid wall no-slip conditions are imposed.

4.3.3. Flow in 4:1 contraction

The 4:1 contraction flow was obviously not considered for its direct applicability to blood flow. The existence of reentrant corners in a region of flow acceleration can introduce singularities in the stress components, making this benchmark convenient for testing the accuracy and stability of numerical schemes.

Case geometry The geometry was set to have the same exit dimension $D = 6.2mm$. The entry cross-section is four times larger. The origin of the coordinate system is in the center of the cross-section, at the point of contraction.

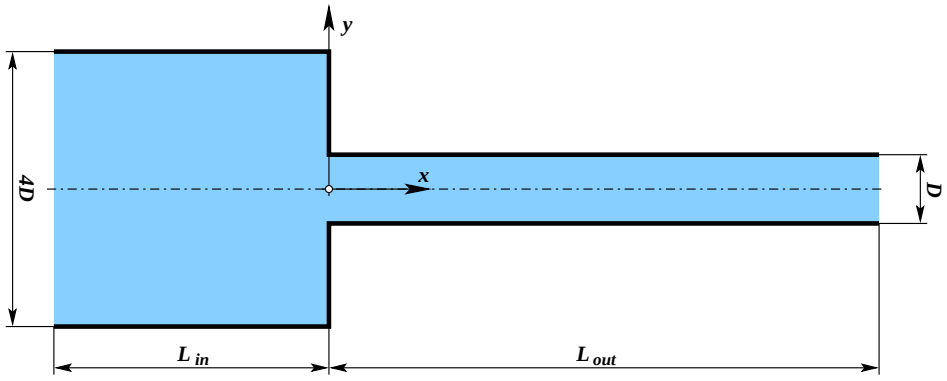


FIGURE 5. Geometry definition for 4:1 contraction case.

Computational grid The grid has about 11000 elements. No special treatment was used to symmetrize the grid with respect to x axis.

https://doi.org/10.1051/mmnp/20149609 Published online by Cambridge University Press

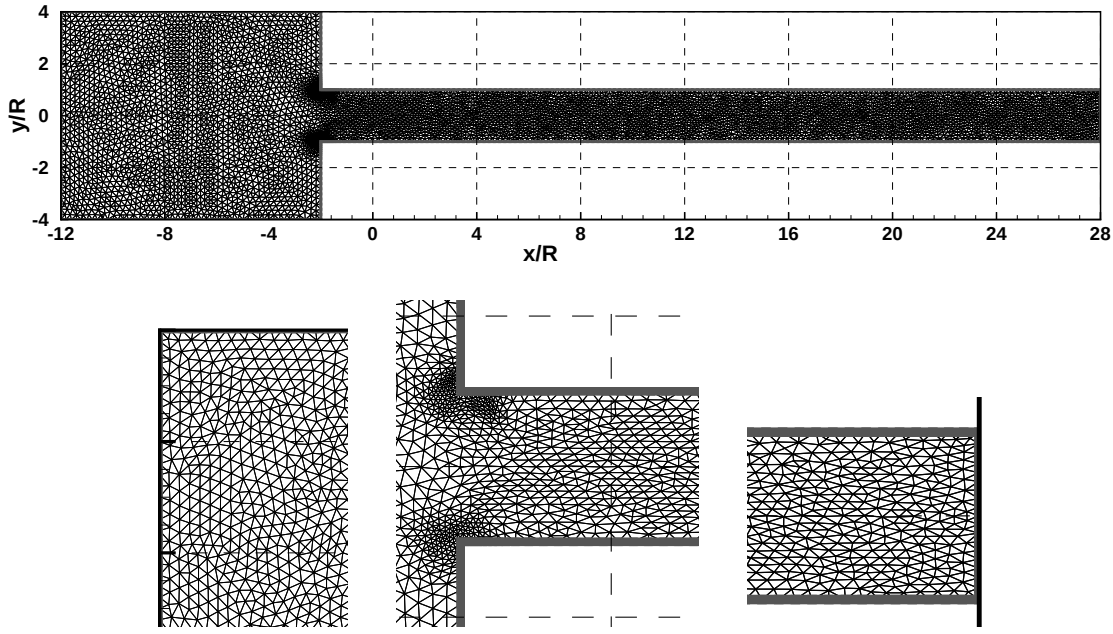


FIGURE 6. Grid for the 4:1 contraction flow.

Boundary conditions Like the corrugated domain, the length of straight inlet pipe is sufficiently long to impose a fully developed Poiseuille flow in the inflow. On the upstream boundary the analytical solution for the fully developed flow in a straight pipe for the respective model are imposed. On the solid wall no-slip conditions are used.

4.3.4. Shear-thinning flow in stenosed vessel

Case geometry The geometry of this test case is two-dimensional version of the stenosed vessel used in [25] or [7] As in the case of the corrugated vessel also here the curvilinear walls have sinusoidal shape. The details of the configuration of the stenosed vessel are shown in the figure 7. The characteristic dimensions

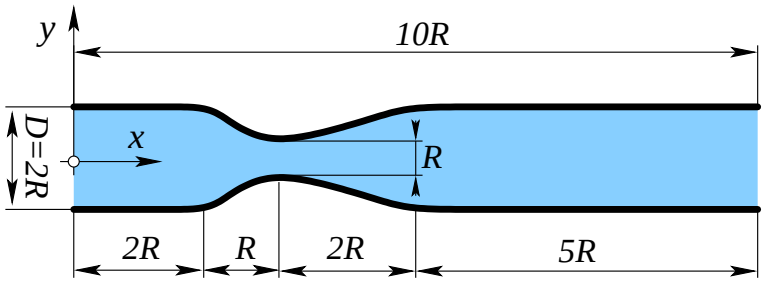


FIGURE 7. Geometry definition for the stenosed vessel case.

used for this case are similar to previous test cases. The diameter (cross-section) size $D = 6.2mm$ is used to define other characteristic lengths.

Computational grid The grid has about 8700 elements. No special treatment was used to symmetrize the grid with respect to x axis.

https://doi.org/10.1051/mmnp/20149609 Published online by Cambridge University Press

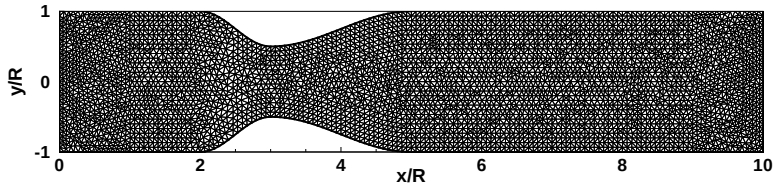


FIGURE 8. Grid for the stenosed vessel case.

Boundary conditions On the upstream inlet boundary the parabolic velocity profile is imposed together with the corresponding Dirichlet boundary conditions for the elastic stress components. On the solid wall no-slip conditions are imposed.

4.4. Numerical Results

The numerical simulations were carried out for a mean velocity $U_0 = 6.15mm/s$, and the reference length was taken as the diameter $D = 6.2mm$, the reference Newtonian (solvent) and elastic viscosities are, $\mu_s = 3.6 \times 10^{-3} Pa\ s$ and $\mu_e = 4.0 \times 10^{-4} Pa\ s$. The constant fluid density is assumed to be $\rho = 1050 Kg/m^3$. Corresponding Reynolds number is $Re = 10$ and relaxation time is $\lambda_1 = 0.06s$ leads to a Weissenberg number $We = 0.06$. Theses values are adapted from those used in [25]. Lower velocity was used to avoid higher Reynolds number and corresponding stabilisation techniques.

Poiseuille flow

The comparison of velocity fields for this case using the traceless and classical model is shown in the figures 9 and 18. The results are expected to be identical for both models.

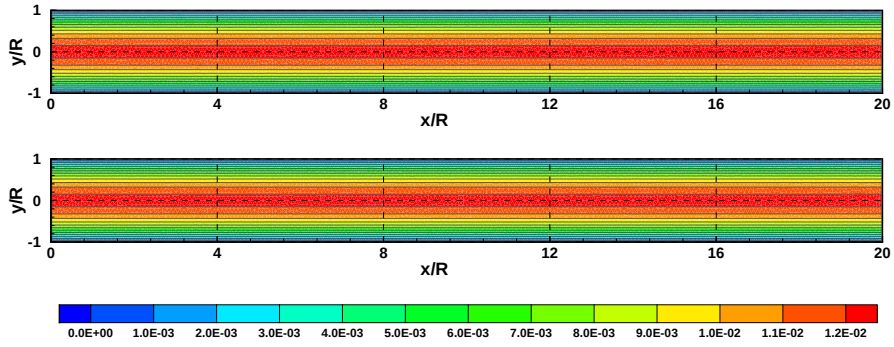


FIGURE 9. Axial velocity (u) contours for the *classical* (top) and *traceless* (bottom) Oldroyd-B model.

The comparison of tensor fields is not as straight forward. The off-diagonal components remain unchanged. For the diagonal components, using the traceless tensor decomposition and definition of elastic pressure, it is possible to convert the results of the traceless model back to the original model notation. The comparison of tensor components (full elastic tensor $\mathbf{T}_e$) is shown in the figure 11[6].

It is important to note that the analytical solution for both the velocity and tensor field components is imposed on the inlet. It perfectly matches the numerical solution obtained in the interior of the domain. This serves as a demonstration of the correctness of the analytical solution for both models for Poiseuille flow.

[6]The color scale is not shown in this side-by-side comparison. It remains the same for both models, however it is different for each tensor component.

https://doi.org/10.1051/mmnp/20149609 Published online by Cambridge University Press

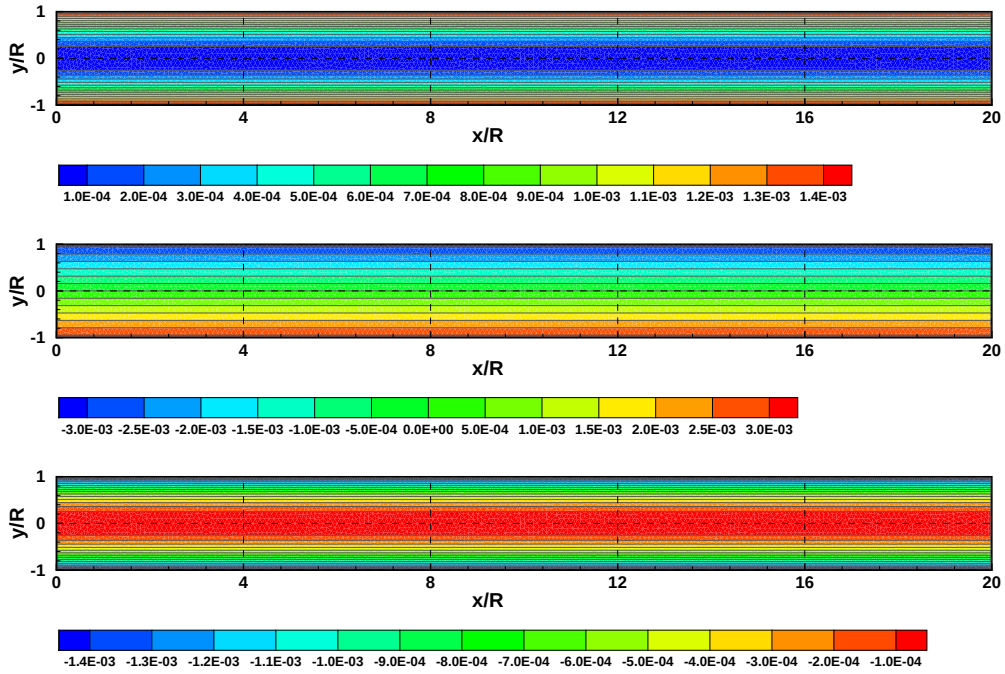


FIGURE 10. Elastic stress tensor components $\hat{t}_1$ (top), $\hat{t}_2$ (middle), and elastic pressure p_e (bottom), for the *traceless* Oldroyd-B model.

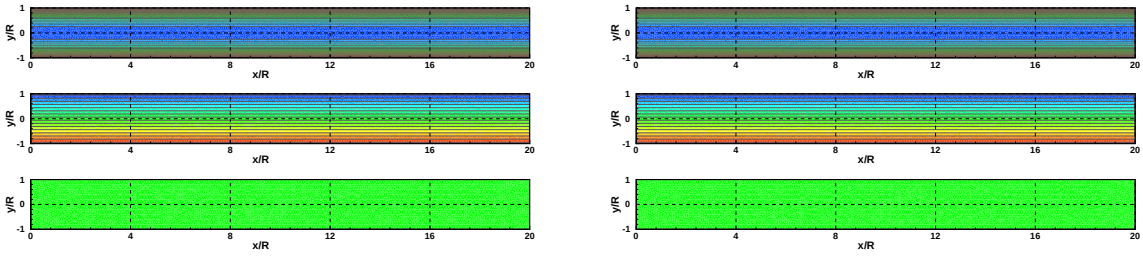


FIGURE 11. Comparison of (full) elastic stress tensor components t_1 (top), t_2 (middle), t_4 (bottom), for the *traceless* (left) and *classical* (right) Oldroyd-B model.

4.4.1. Flow in corrugated vessel

The comparison of velocity and pressure fields for this case using the traceless and classical model is shown in the figures 12, 13 and 14. The results are expected to be identical for both models.

The extra stress-tensor (traceless) and elastic pressure for the traceless model is shown in the figure 15.

The comparison of tensor fields is not as straight forward. The off-diagonal components remain unchanged. For the diagonal components, using the traceless tensor decomposition and definition of elastic pressure, it is possible to convert the results of traceless model back to the original model notation. The comparison of tensor components (full elastic tensor $\mathbf{T}_e$) is shown in the figure 16.

The results for both versions of the model look again the same. The detailed figures reveal that the contours are not as smooth in this case due to much coarser grid used for this test case.

https://doi.org/10.1051/mmnp/20149609 Published online by Cambridge University Press

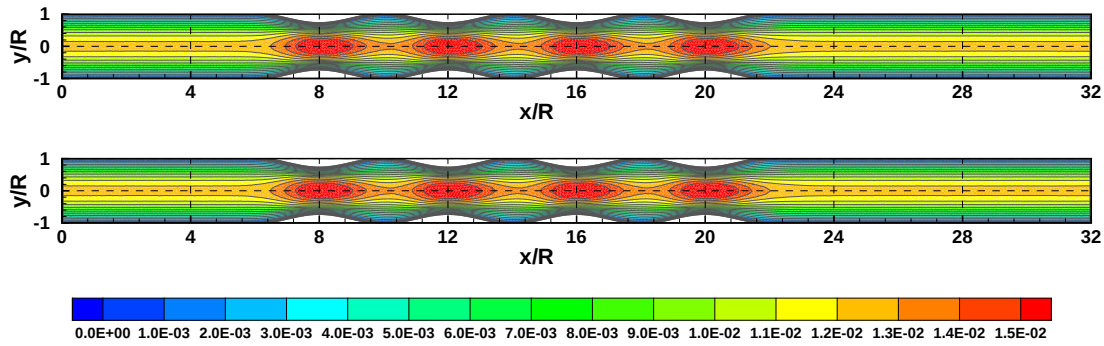


FIGURE 12. Axial velocity (u) contours for the *classical* (top) and *traceless* (bottom) Oldroyd-B model.

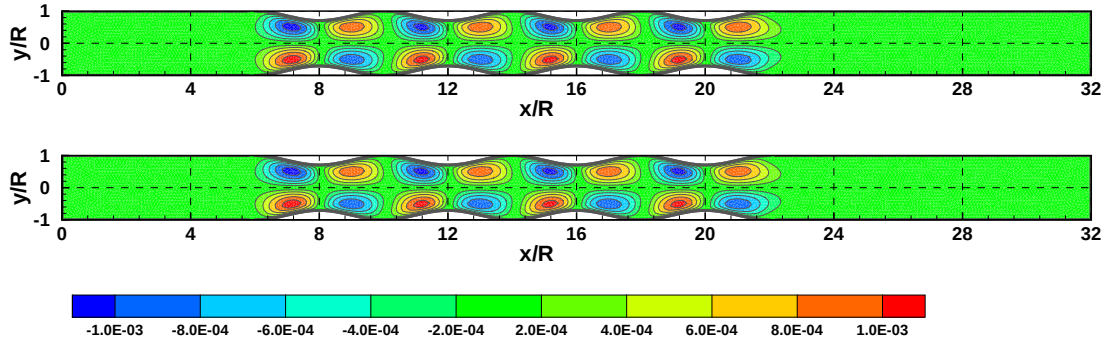


FIGURE 13. Radial velocity (v) contours for the *classical* (top) and *traceless* (bottom) Oldroyd-B model.

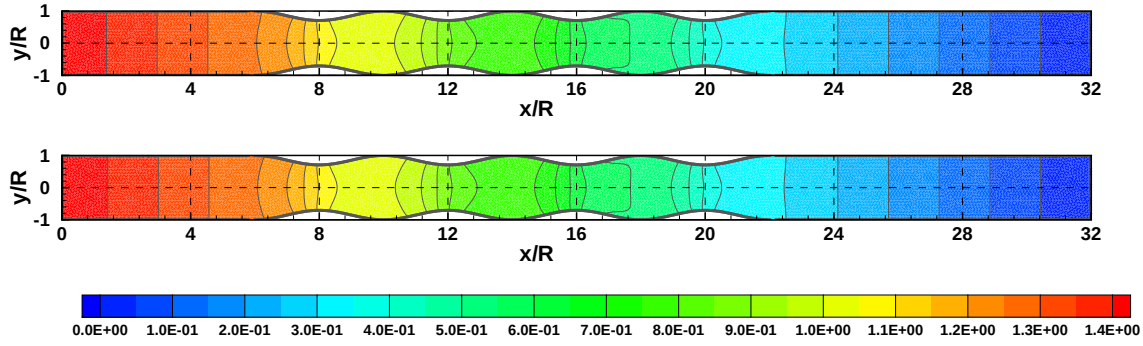


FIGURE 14. Pressure (p) contours for the *classical* (top) and *traceless* (bottom) Oldroyd-B model.

Flow in 4:1 contraction

The comparison of velocity[7] fields for this case using the traceless and classical model is shown in the figures 17 and 18. As for the other cases also here the results are expected to be identical for both models.

The extra stress-tensor (traceless) and elastic pressure for the traceless model is shown in the figure

[7]The characteristic mean velocity is lower than in the other two computational tests to avoid the need of specific stabilisation techniques that are necessary due to high velocity speed-up in the contraction and sharp corners in the domain geometry.

https://doi.org/10.1051/mmnp/20149609 Published online by Cambridge University Press

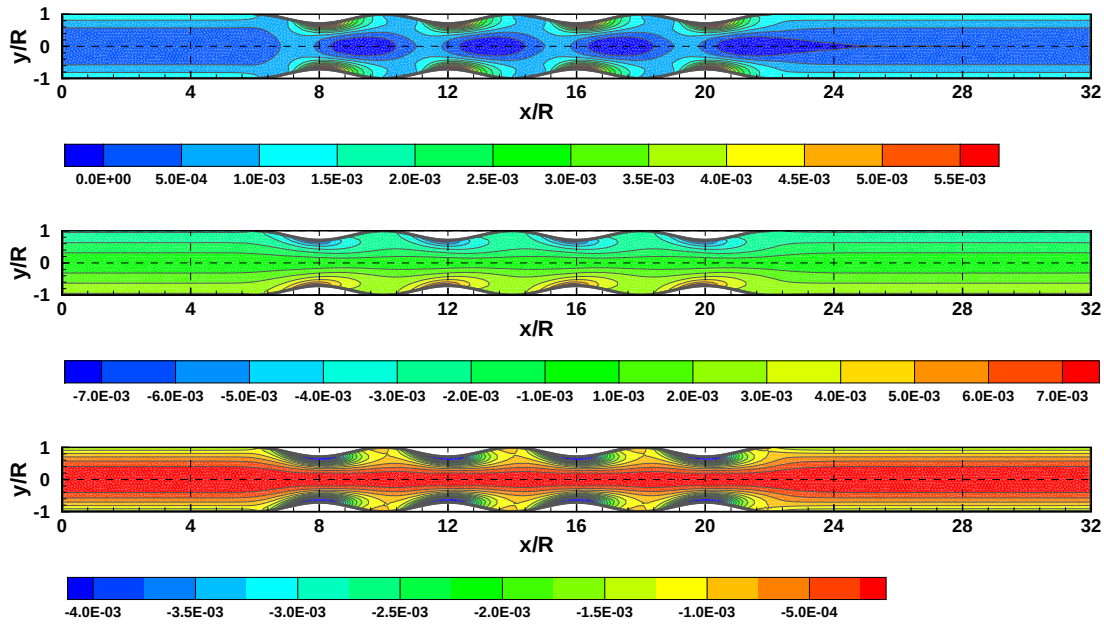


FIGURE 15. Elastic stress tensor components $\hat{t}_1$ (top), $\hat{t}_2$ (middle), and elastic pressure p_e (bottom), for the *traceless* Oldroyd-B model.

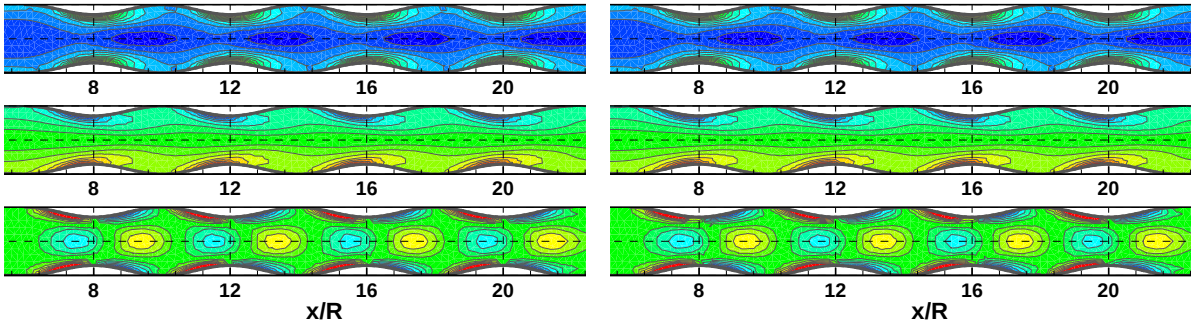


FIGURE 16. Comparison of (full) elastic stress tensor components t_1 (top), t_2 (middle), t_4 (bottom), for the *traceless* (left) and *classical* (right) Oldroyd-B model.

19. The comparison of tensor components (full elastic tensor $\mathbf{T}_e$) is shown in the figure 20. No visible differences were observed in solutions of classical and traceless model. Further simulations for higher velocities (and Reynolds resp. Weissenberg numbers) will be needed to explore the need of stabilisation techniques in the currently used finite-element solver for accurate resolution of the flow around sharp corners in this specific case.

Shear-thinning flow in stenosed vessel

The comparison of velocity and pressure fields for this case using the traceless and classical model is shown in the figures 21, 22 and 23. As in the previous constant viscosity tests, the results are expected to be identical for both models. The extra stress-tensor (traceless) and elastic pressure for the traceless model is shown in the figure 24. The comparison of tensor components (full elastic tensor $\mathbf{T}_e$) is shown in the figure 25.

https://doi.org/10.1051/mmnp/20149609 Published online by Cambridge University Press

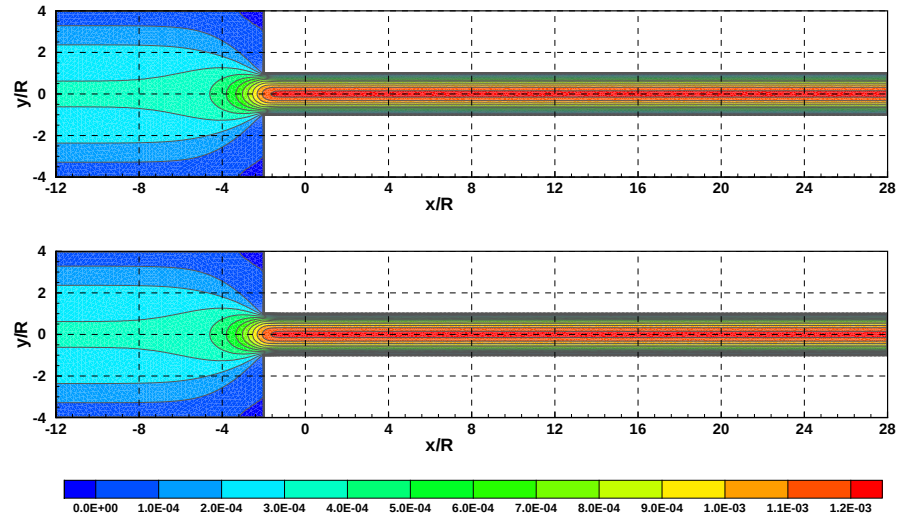


FIGURE 17. Axial velocity (u) contours for the *classical* (top) and *traceless* (bottom) Oldroyd-B model.

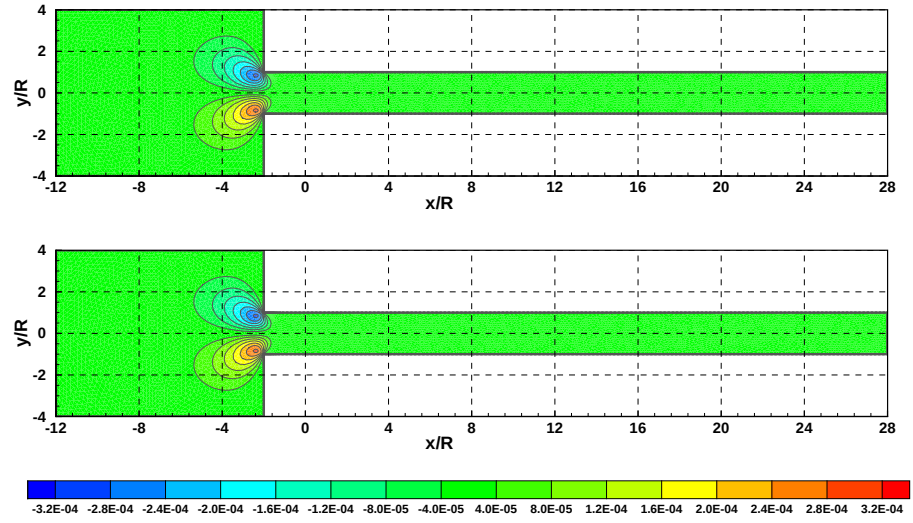


FIGURE 18. Radial velocity (v) contours for the *classical* (top) and *traceless* (bottom) Oldroyd-B model.

As for the previous cases, also here no important differences were observed between the classical and traceless model solution. The variable shear-thinning viscosity does not represent a problem in simulations using the newly developed traceless model.

5. Conclusions and Remarks

From the derivation of the new traceless model follows that a similar decomposition technique can be used not just for the Johnson-Segalman model but also for other viscoelastic models of similar form.

This includes e.g. the generalized Oldroyd and Maxwell models where the constant viscosity or relaxation times are replaced by their variable counterparts. One such example based on the generalized

https://doi.org/10.1051/mmnp/20149609 Published online by Cambridge University Press

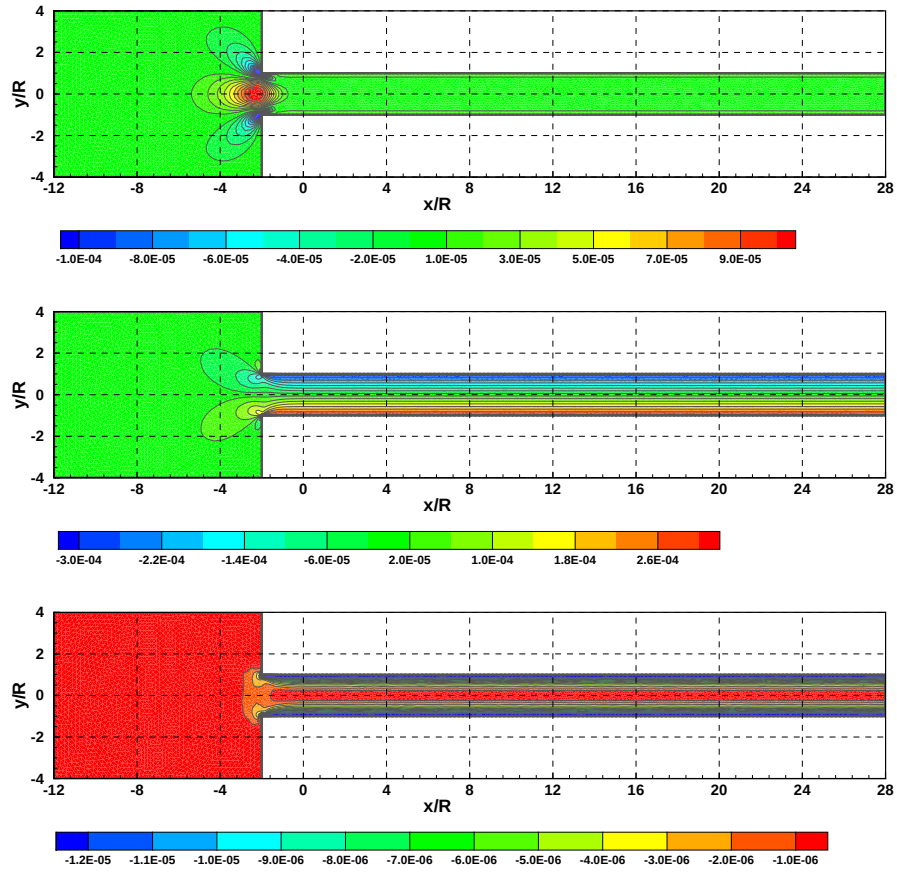


FIGURE 19. Elastic stress tensor components $\hat{t}_1$ (top), $\hat{t}_2$ (middle), and elastic pressure p_e (bottom), for the *traceless* Oldroyd-B model.

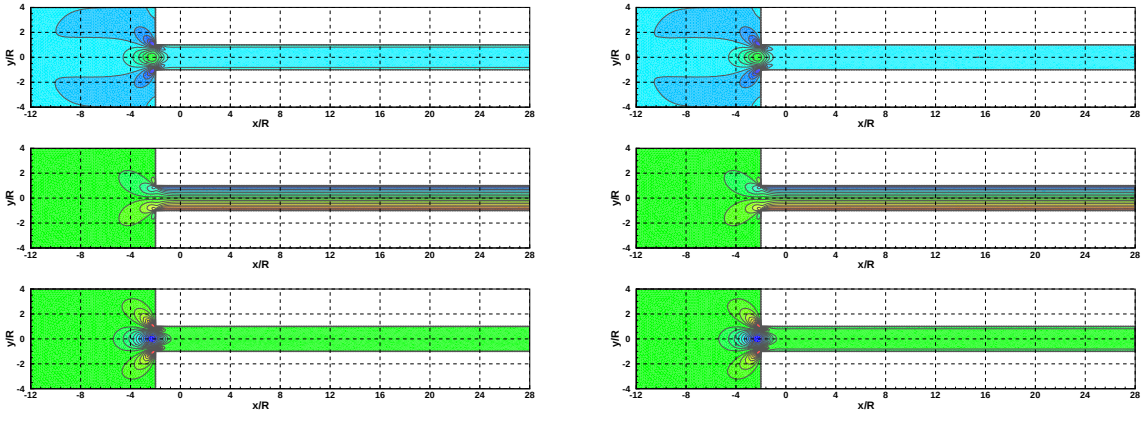


FIGURE 20. Comparison of (full) elastic stress tensor components t_1 (top), t_2 (middle), t_4 (bottom), for the *traceless* (left) and *classical* (right) Oldroyd-B model.

Oldroyd-B model from [25] is shown in the section 3.4. Another example could be the microstructure-based constitutive model for human blood [27], which is nothing else but upper–convected Maxwell model

https://doi.org/10.1051/mmnp/20149609 Published online by Cambridge University Press

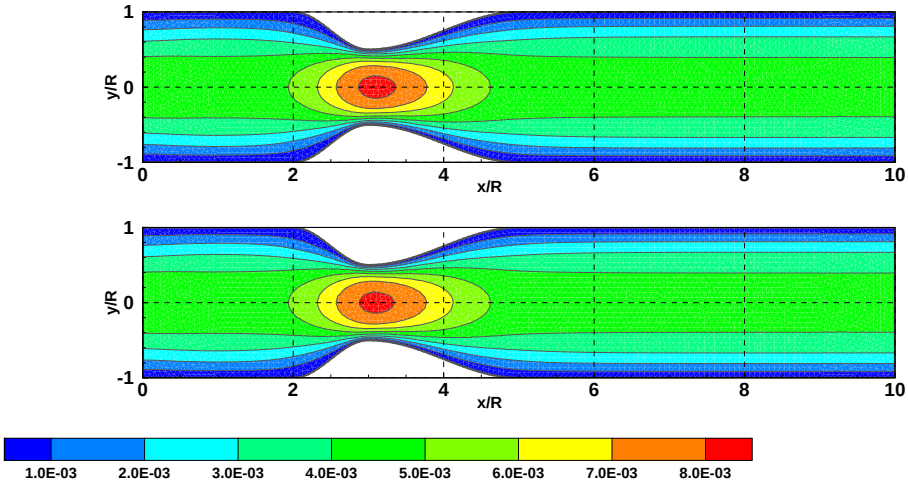


FIGURE 21. Axial velocity (u) contours for the *classical* (top) and *traceless* (bottom) Oldroyd-B model.

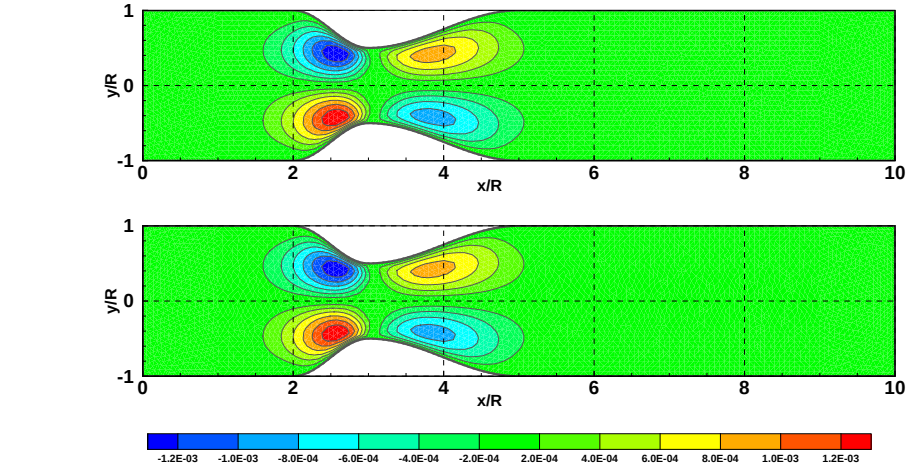


FIGURE 22. Radial velocity (v) contours for the *classical* (top) and *traceless* (bottom) Oldroyd-B model.

with variable (depending on structural parameter) relaxation time. None of these modifications, with respect to constant coefficients models, affect the spherical/deviatoric splitting described in this paper and thus the corresponding generalized models can be modified to traceless versions in the same way as the Johnson–Segalman model discussed here. As a consequence, the traceless decomposition has much wider range of applicability, extending far beyond the Johnson–Segalman model and applications in blood rheology.

The numerical tests have shown the equivalence between the original (classical) and new (traceless) model in terms of model predictions. Since the models are mathematically equivalent, the observed small differences come from the fact that different equations, and therefore different discretizations are being used in each case. The use of analytical solutions for Poiseuille flow as a boundary condition at the inlet has also shown a perfect match between the analytical and numerical solutions for both versions of the Johnson-Segalman model.

https://doi.org/10.1051/mmnp/20149609 Published online by Cambridge University Press

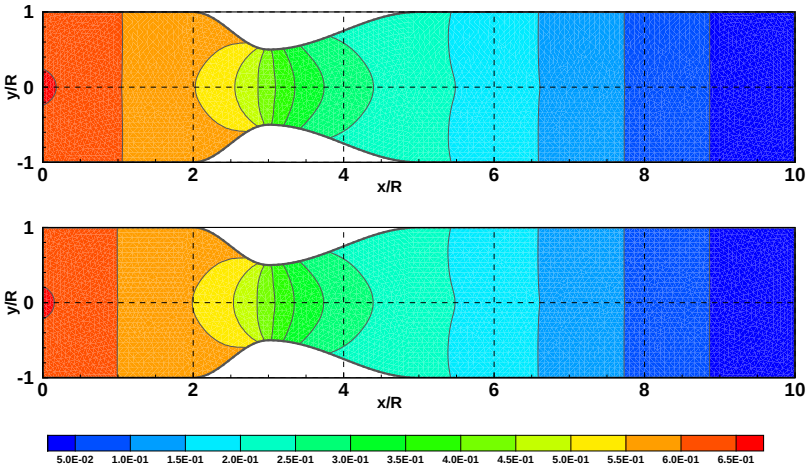


FIGURE 23. Pressure (p) contours for the *classical* (top) and *traceless* (bottom) Oldroyd-B model.

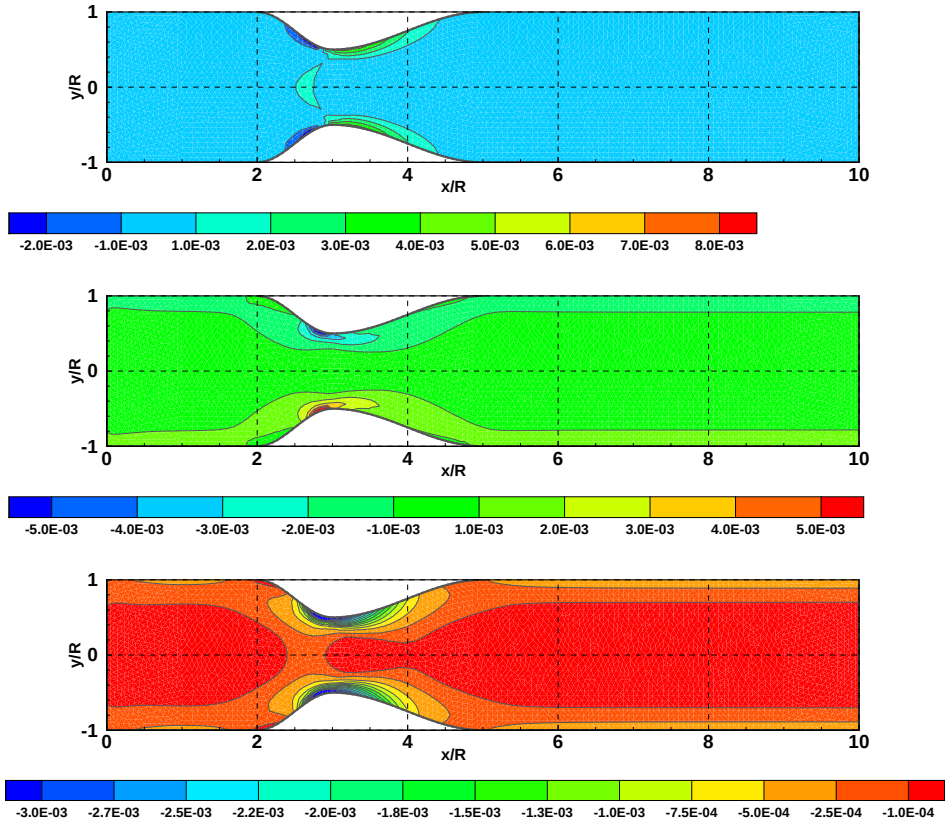


FIGURE 24. Elastic stress tensor components $\hat{t}_1$ (top), $\hat{t}_2$ (middle), and elastic pressure p_e (bottom), for the *traceless* Oldroyd-B model.

Concerning the computational efficiency, both models behave in a very similar way within the range of parameters used for this particular application. Although no rigorous comparison has been made, some

https://doi.org/10.1051/mmnp/20149609 Published online by Cambridge University Press

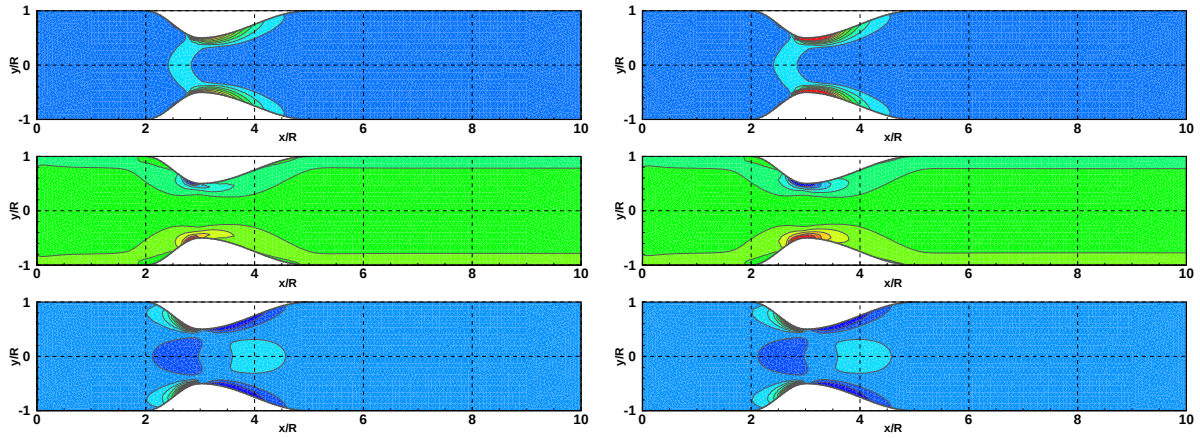


FIGURE 25. Comparison of (full) elastic stress tensor components t_1 (top), t_2 (middle), t_4 (bottom), for the *traceless* (left) and *classical* (right) Oldroyd-B model.

slight advantage of the traceless model is evident. The number of equations to be solved and their type is the same for both models, however the number of terms to be evaluated on the right-hand side of tensor equations is lower for the traceless model. This is even more pronounced in the 2D case in which as noted earlier, some more terms will vanish in the traceless formulation.

The separation of the traceless (deviatoric) and spherical part of stress can be useful in practical applications. E.g. the wall shear stress depends only on the deviatoric part of stress. On the other hand, the vessel wall deformation in some FSI models, depends on the spherical part of stress.

An important question also arises in experimental fluid dynamics. Pressure (and pressure drop) is usually considered as a measurable quantity. If the pressure is defined[8] from the spherical part of the (total) stress, then the corresponding quantity in our model is the sum $p + p_e$. It is good to note that due to the structure of the elastic pressure field, the total pressure is not constant over the vessel cross-section in Poiseuille flow, i.e., the measured pressure value significantly depends on the exact location of measurement point within the cross-section. It is evident that this is typical for viscoelastic models and is in contrast with the Newtonian or generalised-Newtonian fluids models. Translating this back to computational fluid dynamics, it may not be meaningful to make a direct comparison of the pressure (drop) between numerical simulation and experimental data.

Although our simulations have shown that the newly reformulated Johnson-Segalman model is valid and potentially useful, some questions remain to be answered. A whole series of open questions is related to the finite-element implementation of the new model. What should be the choice of finite-elements for the elastic pressure? Should this choice of elements be related to (incompressible) pressure or rather to the tensor components? Is there a stability condition that must be satisfied by the choice of the finite element discretization space for the elastic pressure, similar to the LBB condition for the Newtonian incompressible models?

Other questions concerning the applicability of the decomposed model may arise from specific problems. As an example we can mention the efficiency and robustness of FSI solvers or solution of high Weissenberg number flow problems. In principle there is no reason for the traceless formulation of the model to be a-priori considered superior with respect to the classical version in numerical simulations. The model itself did not change, it was just recasted in a more convenient way. So, in general, the expected computational efficiency, robustness and stability with respect to Weissenberg number is roughly the same. The traceless splitting however opens new possibilities in developing model-specific numerical algorithms (for flow or fluid-structure interaction schemes) that can bring some improvements in these aspects. It also introduces

[8]Also important is the pressure measurement method and corresponding probe design.

https://doi.org/10.1051/mmnp/20149609 Published online by Cambridge University Press

the elastic pressure as a primitive variable of the flow problem, allowing a more direct comparison with experimental pressure measurements.

Some of these topics will be addressed in our future research.

Acknowledgements. The first author is grateful for the funding provided by the Czech Science Foundation under the Grant No.201/09/0917. This work has been partially supported by Projects EXCL/MAT-NAN/0114/2012 and PEst-OE/MAT/UI0117/2011 by CEMAT/IST and CIMA-UE through FCT's Funding Program.

References

[1] M. Anand, K.R. Rajagopal. *A shear-thinning viscoelastic fluid model for describing the flow of blood.* Intern. Journal of Cardiovasc. Medicine and Sci., 4 no. 2, (2004), 59–68, 2004.

[2] N. Arada, M. Pires, A. Sequeira. *Numerical simulations of a shear-thinning Oldroyd-B fluids in curved pipes.* IASME Transactions, 2 no. 6 (2005), 948–959.

[3] N. Arada, M. Pires, A. Sequeira. *Numerical approximation of a viscoelastic Oldroyd-B flows in curved pipes.* In Y. Giga, H. Kozono, H. Okamoto, and Y. Shibata, editors, Kyoto Conference on the Navier-Stokes Equations and their Applications, volume B1 of Kôkyûroku Bessatsu, RIMS, March 2007, 43–70.

[4] N. Arada, M. Pires, A. Sequeira. *Viscosity effects on flows of generalized Newtonian fluids through curved pipes.* Computers and Mathematics with Applications, 53 (2007), 625–646.

[5] R.B. Bird, R.C. Armstrong, O. Hassager. *Dynamics of Polymeric Liquids*, volume I. Fluid Mechanics. John Willey & Sons, second edition, 1987.

[6] R.B. Bird, Ch.F. Curtis, R.C. Armstrong, O. Hassager. Dynamics of Polymeric Liquids, volume II. Kinetic Theory. John Willey & Sons, second edition, 1987.

[7] T. Bodnár, K.R. Rajagopal, A. Sequeira. *Simulation of the three-dimensional flow of blood using a shear-thinning viscoelastic fluid model.* Mathematical Modelling of Natural Phenomena, 6 no. 5 (2011), 1–24.

[8] T. Bodnár, A. Sequeira. *Numerical study of the significance of the non-Newtonian nature of blood in steady flow through a stenosed vessel.* In R. Rannacher and A. Sequeira, editors, Advances in Mathematical Fluid Mechanics, Springer Verlag, (2010), 83–104.

[9] T. Bodnár, A. Sequeira, M. Prosi. *On the shear-thinning and viscoelastic effects of blood flow under various flow rates.* Applied Mathematics and Computation, 217 no. 11 (2011), 5055–5067.

[10] J. Chen, X.-Y. Lu. *Numerical investigation of the non-Newtonian pulsatile blood flow in a bifurcation model with a non-planar branch.* Journal of Biomechanics, 2005.

[11] B. Cockburn, G. Karniadakis, C.Shu. *Discontinuous Galerkin Methods Theory, Computation and Applications*, volume 11 of Lecture Notes in Computer Science and Engineering. Springer Verlag, 2000.

[12] L. Dintenfass. *Blood Viscosity, Hyperviscosity & Hyperviscoaemia.* MTP Press Limited (Kluwer), 1985.

[13] A. Ern, J. Guermond. *Discontinuous Galerkin methods for Friedrichs systems i. general theory.* SIAM Journal of Numerical Analysis, 44 no. 2 (2006), 753–778.

[14] P. Español, X.F. Yuan, R.C. Ball. *Shear banding flow in the Johnson-Segalman fluid.* Journal of Non-Newtonian Fluid Mechanics, 65 (1996), 93–109.

[15] M.M. Fyrillasa, G.C. Georgioua, D. Vlassopoulos. *Time-dependent plane poiseuille flow of a Johnson-Segalman fluid.* Journal of Non-Newtonian Fluid Mechanics, 82 (1999), 105–123.

[16] G.P. Galdi, R. Rannacher, A.M. Robertson, S. Turek, editors. *Hemodynamical Flows - Modeling, Analysis and Simulation*, vol. 37 of Oberwolfach Seminars. Birkäuser, 2008.

[17] A. Gambaruto, J. Janela, A. Moura, A. Sequeira. *Sensitivity of hemodynamics in a patient-specific cerebral aneurysm to vascular geometry and blood geometry.* Mathematical biosciences and engineering, 8 no. 2 (2011), 409–423.

[18] A. Gambaruto, J. Janela, A. Moura, A. Sequeira. *Shear-thinning effects of hemodynamics in patient-specific cerebral aneurysms.* Mathematical biosciences and engineering, 10 no. 3 (2013), 649–665.

[19] F.J.H. Gijsen, F.N. van de Vosse, J.D. Janssen. *The influence of the non-Newtonian properties of blood on the flow in large arteries: steady flow in a carotid bifurcation model.* Journal of Biomechanics, 32 (1999), 601–608.

[20] V. Girault, P.A. Raviart. *Finite Element Approximation of the Navier Stokes Equations*, volume 749 of Lecture Notes in Mathematics. Springer-Verlag, Berlin, 1979.

[21] F. Hecht. FreeFem++ v 3.23 documentation, June 2013. http://www.freefem.org/ff++.

[22] J. Hron, J. Malek, S. Turek. *A numerical investigation of flows of shear-thinning fluids with applications to blood rheology.* International Journal for Numerical Methods in Fluids, 32 (2000), 863–879.

[23] R.W. Kolkka, D.S. Malkus, M.G. Hansen, G.R. Ierley, R.A. Worthing. *Spurt phenomena of the Johnson-Segalman fluid and related models.* Journal of Non-Newtonian Fluid Mechanics, 29 (1988), 303–335.

[24] P. Lesaint, P.A. Raviart. *On a finite element method for solving the neutron transport equation.* In Mathematical aspects of finite elements in partial differential equations, pages 89–123, New York, 1974. Academic Press. (Proc. Sympos., Math. Res. Center, Univ. Wisconsin, Madison, Wis., 1974).

[25] A. Leuprecht, K. Perktold. *Computer simulation of non-Newtonian effects of blood flow in large arteries.* Computer Methods in Biomechanics and Biomechanical Engineering, 4 (2001), 149–163.

[26] B.Q. Li. *Discontinuous Finite Elements in Fluid Dynamics and Heat Transfer.* Springer Verlag, 2006.

https://doi.org/10.1051/mmnp/20149609 Published online by Cambridge University Press

[27] R.G. Owens. *A new microstructure-based constitutive model for human blood.* Journal of Non-Newtonian Fluid Mechanics, 140 (2006), (1–3), 57–70.

[28] K. Perktold, M. Hofer, G. Rappitsch, M. Loew, B. D. Kuban, M. H. Friedman. *Validated computation of physiologic flow in a realistic coronary artery branch.* Journal of Biomechanics, 3 (1998), 217–228.

[29] K. Perktold, G. Rappitsch. *Computed simulation of local blood flow and vessel mechanics in a compliant carotid artery bifurcation model.* Journal of Biomechanics, 28 no. 7 (1995), 845–856.

[30] C. Picart, J.-M. Piau, H. Galliard, P. Carpentier. *Human blood shear yield stress and its hematocrit dependence.* Journal of Rheology, 42 no. 1, 1998.

[31] M. Pires, A. Sequeira. *Flows of generalized Oldroyd-B fluids in curved pipes.* Parabolic Problems, Progress in Nonlinear Differential Equations and Their Applications, 80 (2011), 21–43.

[32] I.J. Rao, K.R. Rajagopal. *Some simple flows of a Johnson-Segalman fluid.* Acta Mechanica, 132 (1999), 209–219.

[33] K.D. Smith, A. Sequeira. *Micro-macro simulations of a shear-thinning viscoelastic kinetic model: applications to blood flow.* Applicable Analysis, 90 no. 1 (2011), 227–252.

[34] G.B. Thurston. *Viscoelasticity of human blood.* Biophysical Journal, 12 (1972), 1205–1217.

[35] G.B. Thurston. *Frequency and shear rate dependence of viscoelasticity of human blood.* Biorheology, 10 (1973), 375–381.

[36] G.B. Thurston. *Rheological parameters for the viscosity viscoelasticity and thixotropy of blood.* Biorheology, 16 no. 3, (1979), 149–162.

[37] G.B. Thurston and N.M. Henderson. Effects of flow geometry on blood viscoelasticity. *Biorheology*, 43 no. 6, (2006), 729–746.

[38] K.K. Yeleswarapu, M.V. Kameneva, K.R. Rajagopal, J.F. Antaki. *The flow of blood in tubes: theory and experiments.* Mechanics Research Communications, 25 no. 3, (1998), 257–262.

[39] F. Yilmaz, M.Y. Gundogdu. *A critical review on blood flow in large arteries; relevance to blood rheology, viscosity models, and physiologic conditions.* Korea-Australia Rheology Journal, 20 no. 4, (2008), 197–211.

https://doi.org/10.1051/mmnp/20149609 Published online by Cambridge University Press